The resonance frequency of tip-vortex cavitation

An Engineering Approach

M.A. Timmer

Faculty of Maritime Engineering

TU Delft Delft University of Technology

Challenge the future

THE RESONANCE FREQUENCY OF TIP-VORTEX CAVITATION

AN ENGINEERING APPROACH

by

M.A. Timmer

in partial fulfillment of the requirements for the degree of

Master of Science
in Marine Technology

at the Delft University of Technology,
to be defended publicly on 16 December 2015 at 9.30 a.m.

Supervisors:	Prof. dr. ir. T.J.C. van Terwisga	
	Ir. P.C. Pennings	
Thesis committee:	Ir. J. Bosschers	MARIN
	Dr. ir. H.J. de Koning Gans	TU Delft
	Dr. ir. M.J.B.M. Pourquie	TU Delft

TU Delft Delft University of Technology

ACKNOWLEDGEMENTS

After quite a few years of spending most my time on my study, this appears to come to an end. At the moment it still feels quite surreal that my main focus will divert from the finalization of my master. However it is about time to take the next step in life, but before that I would like to take the opportunity to express my gratitude towards some people here.

First of all, I would like to thank Mathieu Pourquie for his help in finding a solution to my CFD related problems. Secondly, Tom van Terwisga, who guided me through the last stages of my study. Thirdly, a special thanks goes out to Pepijn Pennings who supported and advised me throughout the last year and a half and was a great source of both information and inspiration. Finally, I would like to express my appreciation to my exam committee in general for their input and advice during progress meetings.

Next to the words of praise for the professional part of my thesis I would also like to express my gratitude to my parents, André and Hetty, for their unabating support to follow through to a successful conclusion of my education. Also a special thank you is reserved for my girlfriend, Annemiek, who stood by me, supported me and motivated me in both good and bad times.

SUMMARY

Over time much research has been performed on the subject of cavitation. A recent development in this field is the investigation into the behaviour of the cavity within a propeller's tip-vortex. It is found that this cavity can produce a very distinct broadband sound-spectrum which can cause trouble on-board ships either by the sound itself or due to the coincidence with the natural frequencies of a ships structure, causing resonance problems. Recent research by Bosschers and Pennings et al. have resulted in an engineering approach to the calculation of a center frequency of this specific type of cavitation sound.

To validate this engineering method, measurements were performed by Pennings [2016] on a 2-bladed propeller in the cavitation tunnel at the Delft University of Technology. The purpose of these measurements was finding the resonance frequency of the tip-vortex cavity. From early measurements it was found that the self-exciting behaviour of the cavity, as it was found by Maines and Arndt [1997], could not be reproduced. To get the cavity to generate sound, an artificial wake was introduced which resulted in the distinct broadband sound-spectrum associated with tip-vortex cavitation. To investigate whether the velocity gradient introduced by the wake is sufficiently steep to excite the natural frequencies of the vortex cavity, velocity measurements have been performed from which a steep dip in the flow velocity was found near and behind the wake generator. Also a highly fluctuating behaviour of the flow, with large deviations from the mean flow, was found. These large spreads are associated with the broadband sound spectrum that comes with tip-vortex cavitation. From this it is concluded that the wake generator, as it is used in the measurements by Pennings [2016], gives a good approximation of a real wake.

To be able to use the engineering method as a tool to predict the center frequency, a method is needed to accurately calculate the cavity radius and the associated circumferential velocity without the need of full scale tests. When such a method is available the resonance frequency associated with tip-vortex cavitation for a specific propeller can be calculated in the design stage of the ship and/or propeller. With this information available an educated trade-off can be made between the alteration of the propeller and the construction of the ship in order to prevent coinciding natural frequencies. To obtain the necessary cavitation information a numerical simulation is performed of which the results show good agreement with measurement data. With this simulation method a relatively fast and accurate prediction can be made of the center frequency of tip-vortex cavitation with the use of the engineering method. However, to grow the confidence in the results produced, further research should be performed.

The current numerical simulations have been performed for a very small propeller. It would be interesting to see whether the method, as it is described and tested in this thesis, also produces good results for a regular scale propeller. Next to that, because the cavity shows no chordwise region over which the parameters of interest are constant, a further investigation into the decay rate of the cavity is advised in order to increase confidence in the choice of location at which the cavitation parameters should be evaluated.

NOMENCLATURE

LDV	Laser-Doppler Velocimetry
PIV	Particle Image Velocimetry
PSD	Power Spectral Density
TDC	Top Dead Center
H_n^1	Hankel function of the first kind
α	Inflow angle relative to rotation plane [deg]
α_g	Geometrical angle of attack [deg]
$\alpha_{L=0}$	Zero-lift angle [deg]
β	Length scale parameter
Γ	Tip vortex circulation [m^2/s]
ω	Angular frequency [1/s]
ρ	Fluid density [kg/m^3]
σ	Cavitation Number
θ	Pitch angle [deg]
c_g	Group velocity [m/s]
c_p	Phase velocity [m/s]
k_r	Radial wave number [1/m]
k_x	Axial wave number [1/m]
r_c	Mean cavity radius [m]
u_θ	Azimuthal velocity [m/s]
V_c	Azimuthal velocity at cavity radius [m/s]
V_p	Rotation velocity of propeller [m/s]
B	Wing span [m]
c	chord at 0.7R [m]
f	Propeller Frequency [Hz]
J	Advance Ratio
Kq	Torque coefficient
Kt	Thrust coefficient
n	Azimuthal wave number [1/m]
R	Propeller Radius [m]
Re	Reynolds Number
T	Surface Tension [Pa m]
U	Free stream velocity [m/s]
W	Mean axial flow velocity [m/s]
z	Camber line offset [m]

CONTENTS

1

INTRODUCTION

OBJECTIVES AND RELEVANCE

Over time much research has been performed on the subject of cavitation. A recent development in this field is the investigation into the behaviour of the cavity within a propeller's tip-vortex. It is found that this cavity can produce a very distinct broadband sound-spectrum which can cause trouble on-board ships either by the sound itself or due to the coincidence with the natural frequencies of a ships structure, causing resonance problems. Recent research by Bosschers and Pennings et al. have resulted in an engineering approach to the calculation of a center frequency of this specific type of cavitation sound.

To validate this engineering method, measurements were performed by Pennings et al. [2015a] on a 2-bladed propeller in the cavitation tunnel at the Delft University of Technology. The purpose of these measurements was finding the resonance frequency of the tip-vortex cavity. From early measurements it was found that the self-exciting behaviour of the cavity, as it was found by Maines and Arndt [1997], could not be reproduced. To get the cavity to generate sound, an artificial wake was introduced which resulted in the distinct broadband sound-spectrum associated with tip-vortex cavitation. To investigate whether the velocity gradient introduced by the wake is sufficiently steep to excite the natural frequencies of the vortex cavity, velocity measurements must be performed.

To be able to use the engineering method as a tool to predict the center frequency, a method is needed to accurately calculate the cavity radius and the associated circumferential velocity without the need of full scale tests. When such a method is available the resonance frequency associated with tip-vortex cavitation for a specific propeller can be calculated in the design stage of the ship and/or propeller. With this information available an educated trade-off can be made between the alteration of the propeller and the construction of the ship in order to prevent coinciding natural frequencies.

SCOPE AND WORK

To get a proper insight in the previous research and its applicability, a review of the literature on the subject is performed and presented in chapter 2. This is mostly focused on the research by Bosschers and Pennings et al. and the engineering method used to calculate the resonance frequency of tip-vortex cavitation sound. To check the effect of the wake generator as was used by Pennings [2016] in the cavitation tunnel, velocity measurements have been performed. The measurement methodology and the effect of the wake generator on the flow are presented in chapter 3. To generate the necessary input variables for the calculation of the center frequency, the radius and circumferential velocity, a numerical simulation has been performed with the purpose of giving an accurate representation of the cavity as it was measured by Pennings [2016]. The method and results are discussed in chapter 4.

2

REVIEW OF LITERATURE

In this chapter a brief overview of the history of research into vortex cavitation will be presented as well as recent developments. Based on this research the development of an engineering model by Pennings et al. [2015b,a] to predict a characteristic frequency of a cavitating propeller aforehand will be presented in more detail.

2.1. HISTORY

Although the possibility of cavitation was already realised by Euler in 1754 and researched by Reynolds as early as 1873, real interest for the phenomenon started at the end of the 19th century with the introduction of the first marine propellers. In 1895 the first mentioning of the term "cavitation" was made by R.E. Froude, the son of William Froude, shortly after the launch of the first high-powered propeller-driven craft "Turbinia" designed by Parsons (Fig. 2.1). This vessel, initially fitted with one gas-turbine and a single two-bladed propeller, was designed to reach a, at that time mind-boggling, speed of 30 knots but reached only about 20 knots in its early test-runs. Parsons realised that the propeller was unable to produce the required thrust due to gas bubbles forming on the suction side of the propeller blades. After experiments with three propellers on a single shaft, he installed three gas-turbines each with a shaft containing three propellers which drove the "Turbinia" to an incredible speed of 32.75 knots. Ever since, the phenomenon of cavitation is extensively researched.

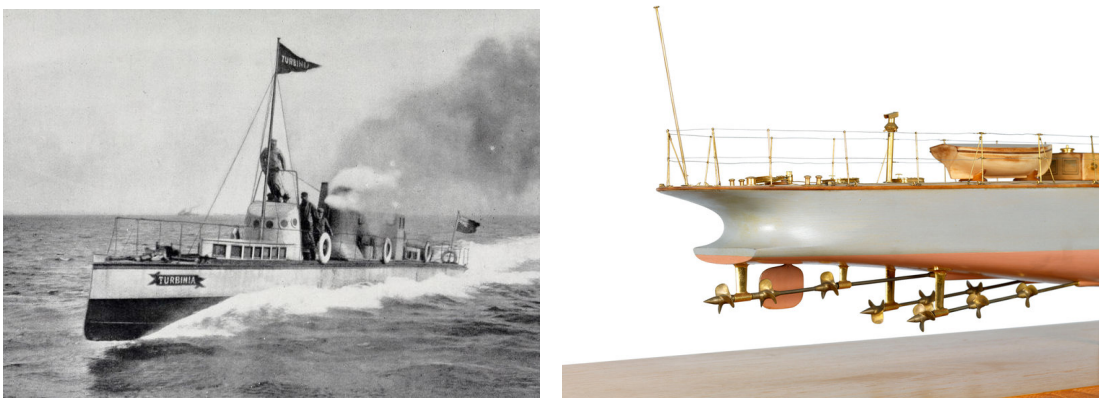

Figure 2.1: Steamship Turbinia at full speed and its propeller array.

2.2. FORMS OF CAVITATION

On a ships propeller, cavitation comes in many forms as is shown in figure 2.2. Each form of cavitation has its own associated problems. A common problem associated with cavitation is erosion of either the propeller or downstream appendages such as the rudder. Another typical aspect of cavitation is the generation of pressure waves which may excite the ships construction or produce audible noise. The cavitation form that is the main interest of this master thesis is cavitation in vortical structures and specifically in the tip-vortex generated by the propeller blade. Therefore a more detailed analysis of this form of cavitation will be given in this section.

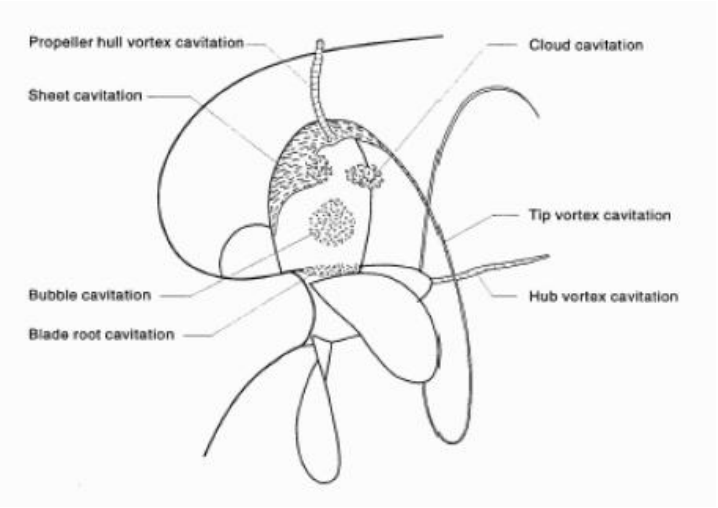

Figure 2.2: Typical types of cavitation on a marine propeller (source: boatdesign.net)

2.2.1. CAVITATION DEVELOPMENT

The primary physical requirement of cavitation is that the local pressure reaches the vapour pressure. When this happens the water boils, turns to gas state and thus forms a bubble in the flow. From a performance viewpoint this might already cause problems, such as the case with the Turbinia (section 2.1) however most problems occur with the implosion of the bubble. Since a cavitation bubble travels with the flow, at some point it will encounter an increase in local pressure which causes it to collapse. When the temporal or spatial pressure gradient is steep, the bubble collapses violently causing shock waves and pressures of up to 10000 times atmospheric pressure resulting in damage to the surface upon which it collapses.
Other aspects associated with cavitation are sound and resonance problems. The pressure waves emitted by the imploding bubbles can travel towards the hull and may excite the ships construction leading to all kinds of sound and vibration related problems. Also the cavity itself can emit sound due to its dynamic behaviour in the flow field which is the case for tip-vortex cavitation. The main part of this chapter will be focused around the calculation of the frequencies emitted by the cavity.

2.2.2. TIP-VORTEX CAVITATION

The existence of a tip-vortex cavity is caused by the centrifugal force on the fluid within the vortex which can be of such magnitude that the vapour pressure is reached in the core of the vortex. This then causes the growth of a cavity. On a well-designed propeller the sheet cavity flows into this same cavity as to prevent cavity collapse on the propeller blade. Due to this connection changes in the magnitude of the sheet cavity also causes changes in the vortex cavity. The interaction of these two forms of cavities is suggested to be the cause of a so called singing vortex as described by Maines and Arndt [1997] where the cavity is self-excited. Recent attempts to recreate this vortex singing by Pennings et al. [2015b] were unsuccessful, therefore an artificial wake was produced using a set of equally spaced plates as shown in figure 3.3. This wake causes the excitation of the eigenfrequencies of the cavity which are associated with the broadband high-frequency noise generated by marine propellers. A detailed analysis of this wake will be given in chapter 3. The broadband behaviour of the vortex cavitation is caused by the variation of the flow and the dynamic behaviour of the cavity itself. Investigation into the origination of the broadband sound spectrum is performed by Bosschers [2009b].

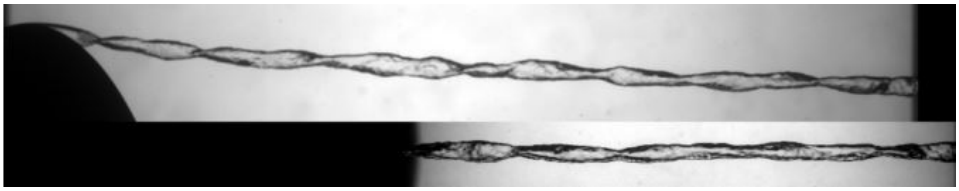

Figure 2.3: Waves on isolated tip-vortex from Pennings et al. [2015a].

In the paper by Pennings et al. [2015b] the relation between the presence of cavitation and the broadband sound spectrum associated with it, is presented. How the center frequency of this sound can be predicted will be discussed hereafter.

2.3. CAVITATION SOUND EMISSION

When one looks closely at the cavity within a tip-vortex it can be seen that waves are present on the cavity, see figure 2.3. Already in the late 19th century this was acknowledged by Lord Kelvin [1880] who also defined a dispersion relation for these waves. The relation was later extended to compressible flow for acoustic analysis by Morozov [1974] and consecutively amended by Bosschers [2008] to accommodate for an inclusion of the axial free-stream velocity. The resulting relation is shown in equation (2.1).

$$\omega_{1,2} = W k_x + \Omega \left[n \pm \sqrt{\frac{-k_r r_c H_n^{1'}(k_r r_c)}{H_n^1(k_r r_c)} T_\omega} \right] \tag{2.1}$$

in which $\Omega = V_c / r_c$ and T_ω corresponds to the contribution of surface tension given by equation (2.2).

$$T_\omega = \sqrt{1 + \frac{T}{\rho r_c V_c^2}(n^2 + k_x^2 r_c^2 - 1)} \tag{2.2}$$

Since the contribution of the surface tension to the frequencies of the vibration modes is very small for the considered cases, this will be omitted. As can be seen from equation (2.1) for each vibration mode n, two frequencies exist corresponding to the plus and minus sign. In future reference these modi will be identified with a plus or minus sign. When the mean axial flow velocity is small compared to the speed of sound than for a sound wave to be emitted the radial wave number squared defined as:

$$k_r^2 = \frac{1}{c^2}(\omega - W k_z)^2 - k_z^2 \tag{2.3}$$

has to be larger than zero resulting in the condition:

$$\left| \frac{c_{p,z}}{c} \right| = \left| \frac{k}{k_z} \right| > 1 \tag{2.4}$$

where $c_{p,z} = \omega / k$ corresponds to the axial phase speed and k is the acoustic wave number in the fluid, $k = \omega / c$. As a result the radial wave number becomes imaginary for small phase speeds or low frequencies and the Hankel function in equation (2.1) reduces to a modified Bessel function of the second kind K. Furthermore, the wave in radial direction becomes an evanescent wave as $k_r^2 \cong -k_x^2$. Finally the dispersion relation for low frequencies is given by:

$$\omega_{1,2} = W k_x + \Omega \left[n \pm \sqrt{\frac{-k_x r_c K_n^{1'}(k_x r_c)}{K_n^1(k_x r_c)}} \right] \tag{2.5}$$

With the dimensionless form defined as:

$$\overline{\omega}_{1,2} = \frac{\omega_{1,2} r_c}{W} = \kappa + \frac{V_c}{W} \left[n \pm \sqrt{\frac{-\kappa K_n'(\kappa)}{K_n(\kappa)}} \right] \tag{2.6}$$

Where $\kappa = k_x r_c \cong i k_r r_c$ is the dimensionless wave number.

In the paper of Bosschers [2008] it is hypothesised that a condition of zero group speed (equation (2.8)) is most likely to cause large cavity deformations. Also the zeroth mode is most likely to generate high amplitude

pressure waves since this is the only mode for which the cavity has volume variations. For this condition the frequency of the n=0^- mode becomes negative corresponding to a negative rotation. Furthermore a relation between the cavitation number and the dimensionless frequency for these conditions is given and compared to the experimental data of Maines and Arndt [1997].

$$c_{p_{1,2}} = \frac{\omega_{1,2}}{k_z} \tag{2.7}$$

$$c_{g_{1,2}} = \frac{\partial \omega_{1,2}}{\partial k_z} \tag{2.8}$$

Pennings et al. [2015a] showed that the dimension-full relation between wave number and resonance frequency, as presented by Bosschers [2009a], coincides with stereoscopic PIV measurements on an isolated vortex cavity. Also a dominant frequency was found to coincide with the zero group velocity criterion of the $n = 0^-$ mode. In conclusion, this method to find a natural frequency of the cavity appears to produce usable figures. However some conditions have to be met which will be set out in section 2.4.

2.4. AN ENGINEERING METHOD

In general it is of interest to be able to predict the frequencies produced by the propeller at an early stage of the design process. That way it is possible to adapt the construction so constructional eigenfrequencies do not coincide with the frequencies excited by the propeller. Part of these frequencies can easily be derived from the propeller frequency. Others, such as those radiated by cavitation, are more difficult to predict. The purpose of the recent research by Bosschers and Pennings et al. is to find an engineering approach to determine a center frequency of the broadband spectrum produced by tip-vortex cavitation during the design stage. This chapter will deal with the input parameters of this approach and its range of applicability.

From equation (2.5) it can be found that the output frequency is a function of $f = \phi(W, k_x, V_c, r_c)$. From this the mean flow velocity, W, is easily calculated. The difficulty lies with the variables that describe the cavity behaviour itself such as the cavity radius and the azimuthal velocity at the cavity radius. Therefore these will be discussed more extensively in the coming sections.

2.4.1. CAVITY RADIUS AND AZIMUTHAL VELOCITY

As stated before there is a relation between the cavity radius and the azimuthal velocity in the form of a balance between outward pointing centrifugal forces and inward pointing pressure forces. Pennings et al. [2015c] found that for the region outside the viscous core of the vortex the azimuthal velocity could be described by the Proctor [1998] vortex model defined as:

$$u_\theta = \frac{\Gamma}{2\pi r}\left(1 - exp\left(-\beta\left(\frac{r}{B}\right)^{0.75}\right)\right) \tag{2.9}$$

where Γ is the strength of the tip-vortex, or half the integrated wing circulation on the blade, B the span of the entire wing and β a length scale parameter that is fitted to experimental data. In this the value of Γ can not easily be calculated for geometries that are non-elliptical and must be calculated with a potential flow solver. In chapter 4 a numerical alternative to find the circumferential velocity and the cavity radius will be presented.

From the known relation of the azimuthal velocity as a function of the radial position, and the knowledge that for cavitation to occur within the vortex, somewhere in the core the vapour pressure should be reached, the cavity radius can be calculated. From the radial momentum equation, with assumed axisymmetry and zero radial velocity defined as in equation (2.10) and the cavitation number defined as in equation (3.2) the cavity radius can be found. In equation (2.11) the solution that needs to be solved to find r_c is presented from which the only unknown is the cavity radius. This equation can be solved numerically.

$$\frac{dp}{dr} = \rho\frac{u_\theta^2}{r} \tag{2.10}$$

$$P_\infty - P_v = \rho\int_{r_c}^{\infty}\frac{u_\theta^2}{r}dr \tag{2.11}$$

Finally a unique relation per mode between the wave number and the oscillation frequency exists as was shown by Bosschers [2009a]. Through finding the condition of zero group velocity for the $n = 0^-$ mode the center frequency of the broadband sound spectrum related to tip-vortex cavitation can be found.

The steps taken in the above analysis of the center frequency of the cavity sound spectrum are graphically presented in figure 2.4.

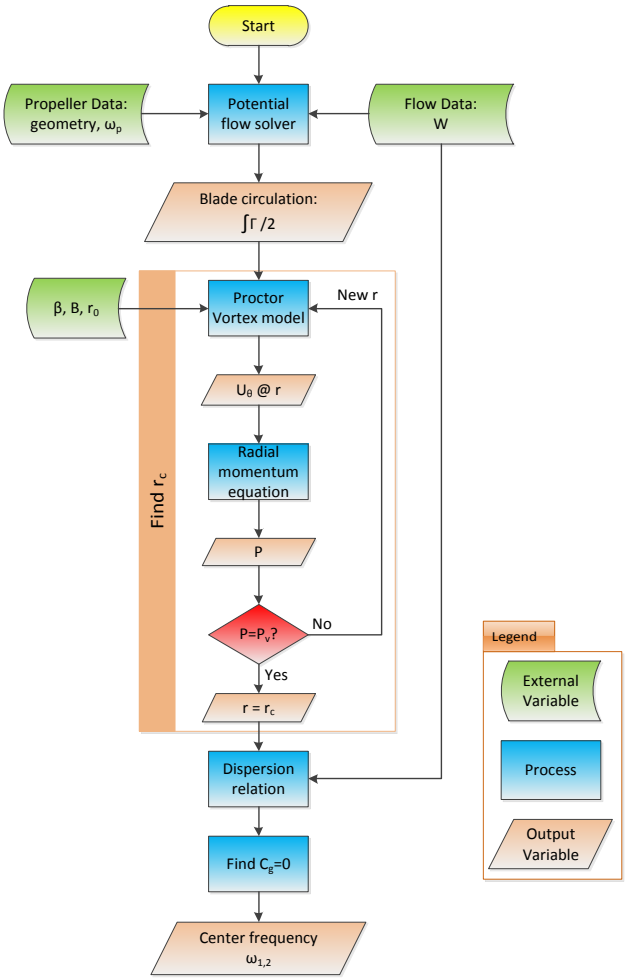

Figure 2.4: Graphical representation of the calculation process involved in finding the center frequency of the tip-vortex cavity sound spectrum

2.5. DISCUSSION

For the current calculation scheme a number of assumptions have been made to be able to create a complete model. Since the cavitation behaviour exists largely due to the fluid viscosity it is contradictory to use a potential flow solver to find the mean circulation on the propeller blade. However from literature (e.g. Anderson [1991]) it can be found that the circulation of a wing defined in a potential flow, using the Kutta-condition at the trailing edge is very similar to the wing circulation in a viscous flow. Also, the dispersion relation is derived for potential flow but the azimuthal velocity contribution is calculated with a viscous vortex model. Here Pennings et al. [2015c] showed that for radii outside the viscous core, the circumferential velocity prediction of the Proctor model coincides with the results from PIV measurements when the fit parameter β is chosen correctly. Therefore the viscous flow model of a non-cavitating vortex can be used as a method of finding the cavity size and pressure where it should be noted that the value of β is derived from experimental data and that the generality of its value should be investigated further.

3

WAKE VELOCITY MEASUREMENTS

As part of his Phd research Pennings et al. [2015b] has performed cavitation measurements in the cavitation tunnel at the Delft University of Technology. He investigated the cavitation behaviour of a propeller in both a uniform inflow as well as a situation where the inflow is disturbed by a wake generator. For the case of uniform inflow the flow velocities are known, for the case with wake the velocity is however unknown. To get an idea of the flow velocities behind and near the wake generator, measurements have been made. This chapter will further discuss the purpose of these measurements in section 3.1 and the measurement methodology in section 3.2. Finally the outcome of the measurements will be discussed and presented in section 3.3.

3.1. PURPOSE OF VELOCITY MEASUREMENTS

From visual investigation it already becomes very clear that the influence of the wake generator is significant. In figure 3.1 this effect can clearly be seen. Both pictures are taken in the same angular position at the same propeller loading and cavitation number, namely $J = 0.56$ and $\sigma = 0.40$. The definitions of these values can be found in equations (3.1) and (3.2) where V is the sum of the contributions of the flow velocity and the rotational velocity of the propeller.

$$J = \frac{U}{nD} \tag{3.1}$$

$$\sigma = \frac{P_\infty - P_v}{\frac{1}{2}\rho V^2} \tag{3.2}$$

The right hand side picture shows a significantly larger sheet cavity than the left hand side picture. Also a clear disturbance of the tip vortex cavity in the downward flow field is visible. Both effects can be attributed to the presence of the wake generator.

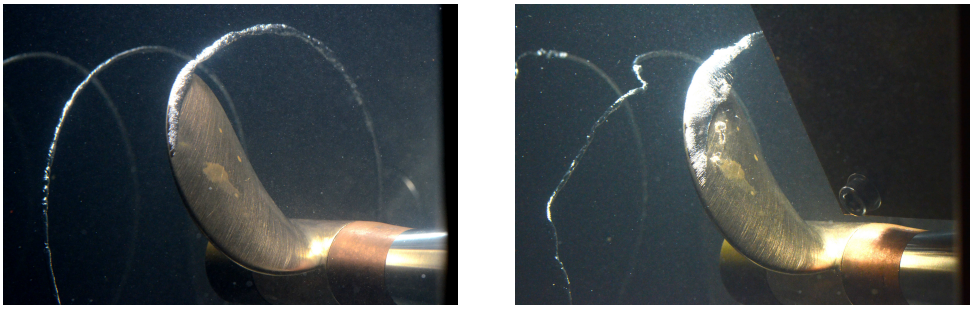

(a) Uniform Inflow (b) Inflow with wake

Figure 3.1: The influence of a disturbed flowfield on the cavitation behaviour of a propeller.

The presence of a wake does not only influence the visual behaviour of the cavitation on the blade and cavity emanating from the blade, it may also influence the acoustical behaviour of the vortices. As was described in chapter 2 the tip-vortex cavity can generate sound when it is excited in its natural frequencies. When the rate of change of the flow velocity near the wake generator is sufficiently large, than one or more of the tip-vortex cavities eigenmodes can be excited and it will start producing audible sound. This is the main focus of the research of Pennings et al. and Bosschers.
The set-up as is shown on the right hand side of figure 3.1 was used by Pennings et al. [2015a] for his research into the behaviour of cavitating vortices. During the tests a clear sound could be heard and was also recorded. Further investigation showed that the sound covered a broad range of frequencies and had no obvious relations to the blade passage frequency. It was therefore concluded that this was the broadband sound spectrum that was considered to be related to the sound emitted by a cavitating tip-vortex. As a result, the effect of the disturbed flow field in the vicinity of the wake generator is of interest to be able to determine whether the wake is deep enough to be the cause of the excitation of the eigenmodes of the tip-vortex cavitation.

3.2. MEASUREMENT METHODOLOGY

3.2.1. INSTRUMENTATION

The flow velocity measurements for the flow with wake generator are performed with a Pitot tube. This instrument is chosen because of the ease of measuring and because only the streamwise velocity is of interest. Therefore no highly sophisticated measurements methods such as PIV or LDV are necessary to get accurate measurements.
Whilst the tunnel is filled with water, only the radial position of the tip of the Pitot tube can be changed and therefore, to make a proper measurement grid, the wake generator should be rotated around the propeller shaft it is mounted on. The measurement layout for one angle is shown in figure 3.2.

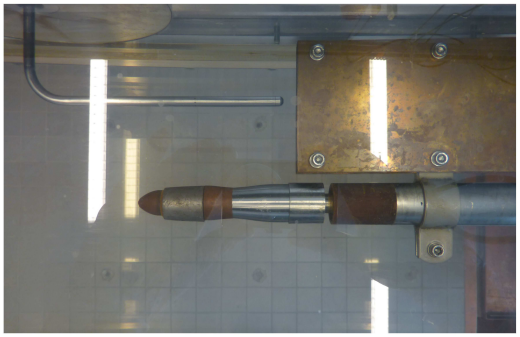

Figure 3.2: Topview of the measurement layout with Pitot tube and wake generator mounted on the tunnels propeller shaft.

3.2.2. CAVITATION TUNNEL

The cavitation tunnel in the Laboratory for Ship Hydromechanics at the Delft University of Technology has a test section area of 0.30 $\times$ 0.30 m^2 which increases vertically in streamwise direction to 0.30 $\times$ 0.32 m^2 to compensate for the boundary layer growth and ensures no streamwise pressure gradient is present.

For the flow velocity of the tunnel is subject to sudden unexplained oscillations, Pennings et al. developed a program to control the flow velocity based on the pressure drop over the contraction of the cavitation tunnel. This pressure drop is measured with a differential pressure sensor (Validyne DP15 with membrane No. 36) and the flow velocity is adapted by controlling the RPM of the tunnel drive.

3.2.3. CONDITIONS

The head of the Pitot tube used for the velocity measurements is located 10 mm behind the wake generator. This distance is chosen since this also was the distance between the wake generator and the closest edge

of the propeller and therefore it is considered to be representative for the actual velocities encountered by the propeller. The velocity is measured as the difference between the static and the dynamic pressure and is measured with a number 28 membrane in a Validyne DP15 pressure difference sensor. The membrane has a pressure range up to 5.5 kPa which is considered to be sufficient for the chosen flow velocity of 3.2 m/s. This flow velocity is one of the conditions that where used by Pennings [2016] and suffices for a fully turbulent Reynolds regime for the current test set-up.
The dimensions of the wake generator are shown in figure 3.3. These dimensions and the flow velocity of 3.2 m/s result in a Reynolds number of $Re \sim 10^6$ (equation (3.3)). The wake generator itself is build up of 5 equally spaced metal plates as can be seen in figure 3.3. The spacing between the plates enables some water to flow through. However at the positions where the plates are bolted together anomalies occur which will be further discussed in section 3.2.4.

$$Re = \frac{\rho V L}{\mu} \tag{3.3}$$

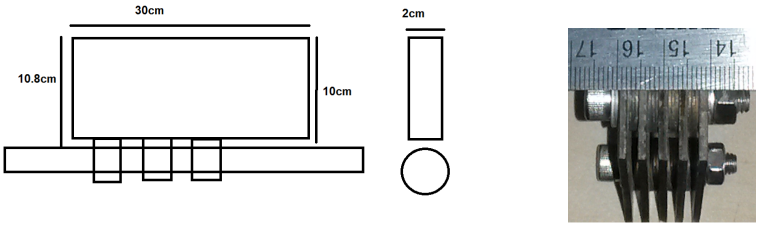

(a) Dimensions of the wake generator

(b) Wake generator topview

Figure 3.3: Wake generator dimensions (a) and layout (b)

3.2.4. MEASUREMENTS

As a preliminary investigation into the dimensions of the wake a coarse measurement grid is generated. The resulting velocities as well as the locations of the measurement points are shown in figure 3.4. The iso-velocity lines in this figure are coarse estimates of the actual velocity profile. They do however give a good indication of the effect of the wake generator on the flow velocity and give a good basis for a refined measurement grid.

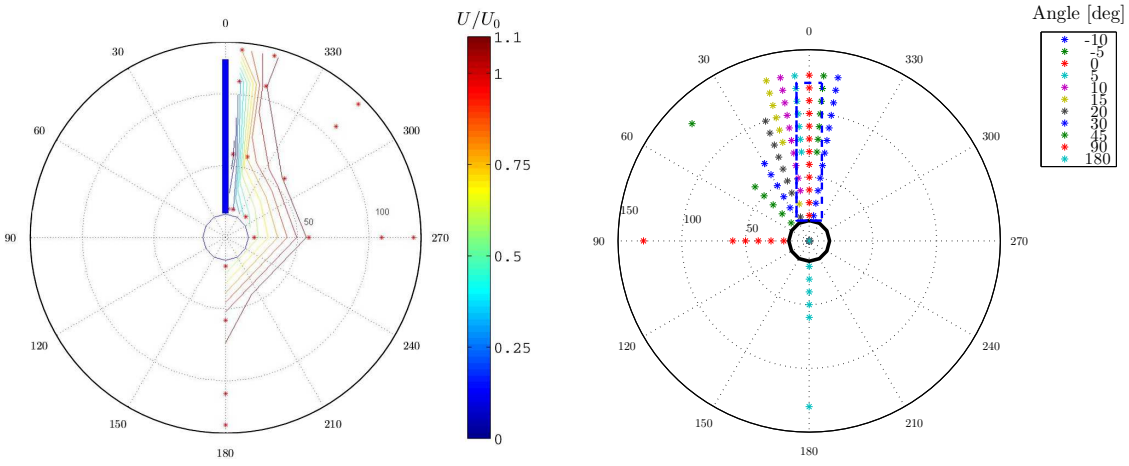

(a) Results of initial measurements in [m/s]

(b) Final Measurement grid

Figure 3.4: The asterisks denote the points where the velocity is measured. The coloured lines in the left plot are iso-velocity lines. The thick blue line shows the position of the wake generator whereas the black circle shows the position of the propeller shaft.

Based on the initial measurements it is clear that the grid refinement should mostly take place in the area close to the wake generator, since these measurements show that at a distance of about 30 mm away from the plates the flow remains at the free stream velocity. So the layout of the measurement grid was defined as is shown in figure 3.4. As was already mentioned, once the tunnel is filled only radial steps can be taken to measure the velocity in multiple points. To measure at multiple angles the tunnel is partially drained and the wake generator is rotated around the shaft to an angle relative to the position of the Pitot tube mounting. Therefore the grid in figure 3.4 is defined in radial and angular coordinates. The radial spacing of the grid points is 10 mm. The minimum distance between points of successive angles is set to 6 mm. This results in a more or less equally spaced grid.

For each angle and radial position measurements are taken for a duration of about two minutes. From the results of the initial measurement it was found that this duration is sufficient for the calculation of a converged mean and standard deviation of the velocity.
At the beginning of each day of measurements a zero measurement was performed with a fully filled tunnel without flow. These measurements are used to remove any offset from the measurement data that is present in the sensors.

During the measurements problems occured at the points where the plates of the wake generator are bolted together. Behind the plates and behind the outward ends of the bolts, negative velocities where measured. Although the principle of the Pitot tube is not appropriate to measure negative velocity it does indicate that the dynamic pressure is smaller than the static pressure and thus there is a no streamwise flow. The magnitude indicated by the pressure sensor is however very unreliable and these measurements are therefore discarded in the post-processing of the data.

3.3. RESULTS

Already from the initial measurements it became clear that the flow velocity in the vicinity of the wake generator is significantly reduced. The measurement on the refined grid uphold these findings. In the present section the measurement result will be presented and discussed.

The velocity in the wake is subject to large fluctuations, especially near the edge of the wake generator, resulting in a large standard deviation in the measurement signal. This non-steady behaviour of the flow is consistent with findings by Pennings et al. who already found that the cavitation behaviour of the propeller was irregular from one rotation to the other as is shown in figure 3.5.

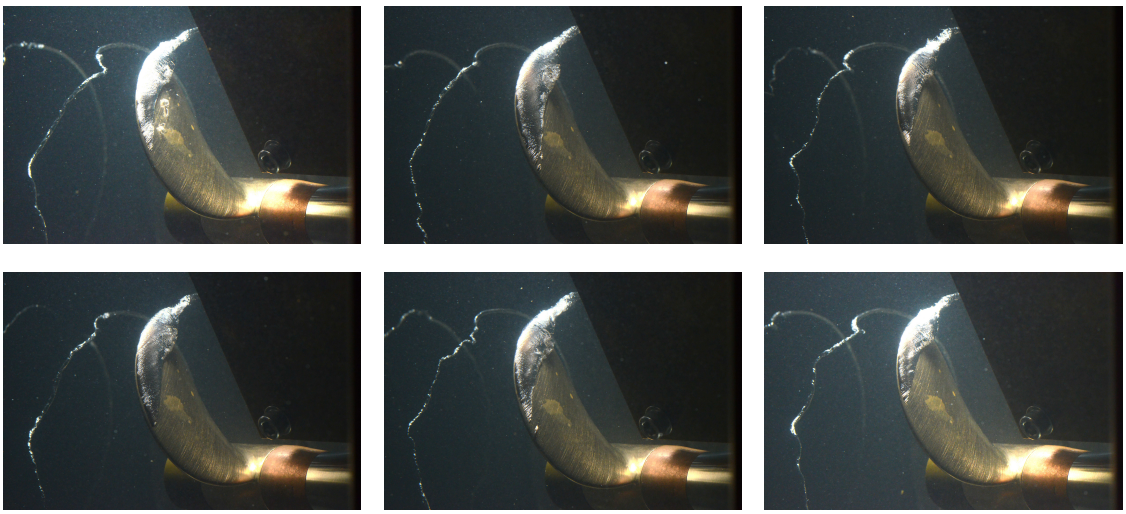

Figure 3.5: Cavitation behaviour at identical conditions at different moments

From the measurements it becomes clear that the flow velocity close to the wake generator, but not behind, is most susceptible to these irregularities. A plot of the measured flow velocities in each location and

the variance of the measured signal is shown in figure 3.6. In this plot the colour of the squares indicates the velocity. The size of the squares is related to the variance (σ^2). Finally, the blue dotted line and the black circle indicate the geometry of the test set-up.

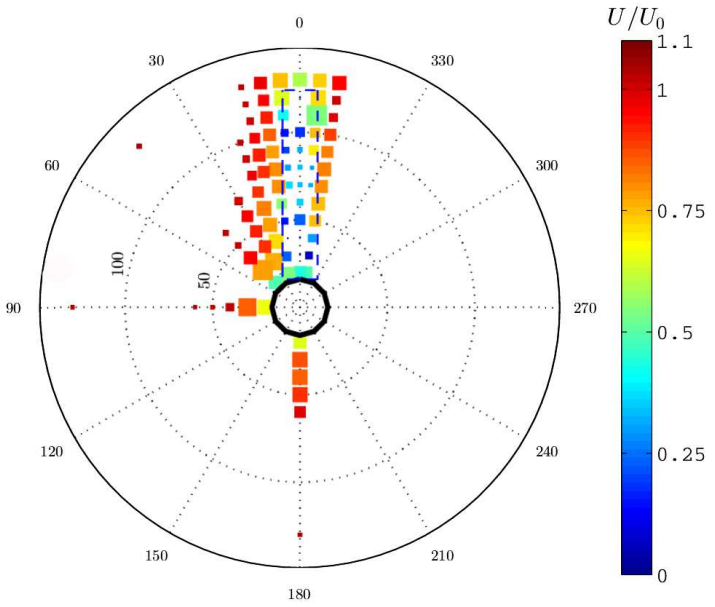

Figure 3.6: Results of flow measurements. The colour of the squares indicates the velocity and the size of the square is related to the variance.

The figure evidently shows that the flow velocity behind the plates and close to the plates is decreased and that away from the plates the flow velocity quickly returns to the mean flow velocity. Furthermore, the flow appears to be symmetrical at both sides of the wake generator. The flow velocity directly behind the plates is much lower than the ambient flow and is quite constant in magnitude, except close to the bolt positions. So clearly a small but steady flow goes through the wake generator.
One thing that is not indicated in this figure although it is part of the test set-up, are the brackets with which the wake device is mounted on the tunnel shaft. In figure 3.2 one of these brackets is visible and clearly protrudes into the flow at the opposite site of the shaft. This causes the flow irregularity to extend further from the shaft at the 180^0 position than at the 90^0 angle. This effect can be seen in figure 3.6.

With the assumption that the velocity profile around the wake generator is symmetrical, the velocity can be plotted as a function of the distance perpendicular to the plates centreline. For this, all points that may be influenced by discontinuities in the generators geometry, such as near the locations of the bolts, are removed. Also points that are positioned radially outwards of the device are deleted. Measurement points that lie very close to the tunnels propeller shaft are also removed from the graph since the velocity here might be affected more by the presence of the shaft than by the wake device. Finally, only the data for angles ranging from -10^0 to $+45^0$ are taken into account. The remaining measurements are grouped based on their distance perpendicular to the plates centreline. Per group a mean value and a standard deviation is plotted. From figure 3.7 it is evident that the velocity fluctuations in the wake near the edge of the wake generator are very large compared to the fluctuations in the rest of the wake where the outer edge of the wake generator is represented by the black dash-dotted line. The figure shows that outside of the geometric range of the wake device, the flow velocity quickly returns to the free stream velocity in the tunnel and thus a sharp gradient is present near the edge of the wake generator. Since this sharp gradient is required for the excitation of the tip-vortex cavity it is convenient that the design of the wake generator fulfils this requirement. A further review of the wake shape and its effects on the flow and cavitation behaviour will be given in section 3.4.

Together figures 3.6 and 3.7 give a clear insight into the effect the wake generator has on the flow. It is apparent that the effect of the device is localised close to itself and that the flow in other parts of the tunnel is only disturbed by secondary effects, such as by the mounting brackets.

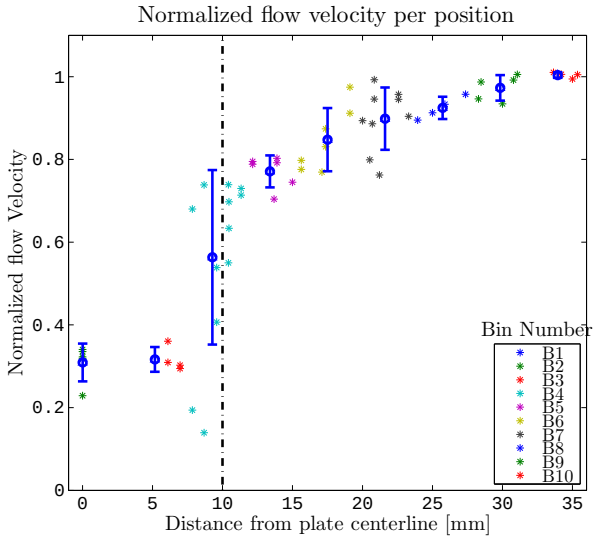

Figure 3.7: Binned velocities close to wake generator. The vertical black line indicates the edge of the wake generator. The blue mean values and errorbars are the mean and standard deviation of each velocity bin.

3.3.1. BLOCKAGE EFFECT

The velocity that was chosen at the start of the experiment was based on an empty tunnel and thereafter the flow velocity at the end of the tunnels contraction was kept constant. From the measurement results it was found that the free stream velocity with the wake generator was not $3.2 m/s$ but slightly higher at about $3.3 m/s$. It is thought that the blocking effect of the wake generator causes the flow velocity to decrease locally, since the mass transport is kept constant at the end of the contraction, the velocity in the remainder of the flow field has to be higher to accommodate the same net mass transport over the measurement plane.
In figure 3.8 the influence of the wake generator is shown. The velocity profile that is plotted for the case with wake generator is the measurement series at a 90^0 angle, so perpendicular, to the generator. For this angle the area that is directly influenced by the plates, is smallest. It can however be seen that for small radii the flow velocity is still disturbed by the wake generator.

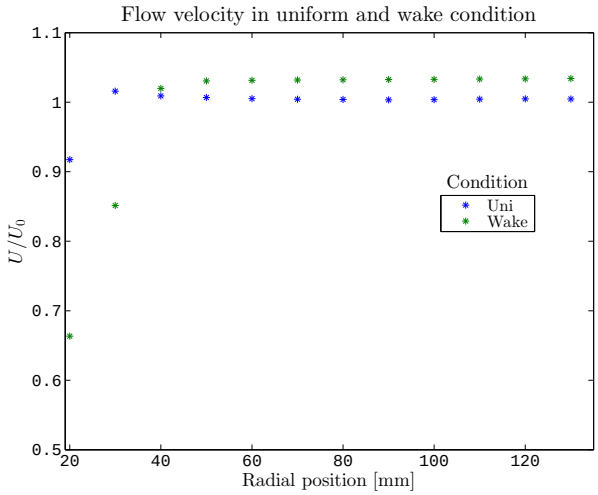

Figure 3.8: Influence of the wake generator on the flow velocity per radial position.

The velocity in the outer region, at radii larger than 40 mm, of the flow with wake generator, is higher than the flow without it. When an integration of the volume flow over the entire plane is made, the mass transport for the uniform flow and the wake induced flow are equal. This shows that the increase in velocity in the outward flow region is indeed the result of blockage of the wake generator.

3.4. IMPLEMENTATION OF MEASUREMENTS

In the previous section it was shown that the flow velocity in close proximity to the wake generator is significantly retarded. Also it was mentioned that the steepness of the velocity gradient is of influence on the excitation of the vortex cavity. In this section this influence and its relation to the velocity gradient will be covered.

3.4.1. ENCOUNTERED WAKE

When the propeller blade travels through the wake it encounters a changing inflow velocity due to the reduced flow velocity near the wake generator. As an effect the inflow angle and therewith the loading of the propeller blade changes during its rotation. When the flow velocity encountered by the propeller blade is presented as a recurring dimensionless block wave, it is possible to perform a spectral analysis on it. The velocity is made dimensionless via division by the free stream flow velocity in the tunnel without the wake generator.

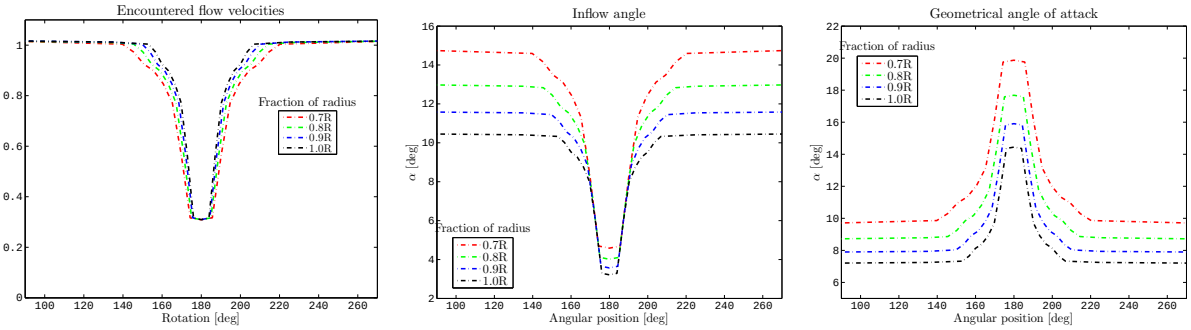

(a) Encoutered dimensionless flow velocities

(b) Inflow angle on propeller blade

(c) Geometric angle of attack

Figure 3.9: Encountered flow conditions during one rotation of the propeller at several radii

For the remainder of the analysis it is assumed that in the region of interest, at the outer radii of the propeller, the profile of the wake perpendicular to the wake generator is constant over the radii. Since this region is free of geometrical disturbances and relatively far from the propeller shaft it is thought to be accurate. Consequently the mean flow velocities found from figure 3.7 can be used. The encountered velocity profile for four radii are plotted in figure 3.9. In this figure the encountered flow velocity is again made dimensionless with the undisturbed flow velocity in a situation without wake inducer. The rotation angle of 180^0 coincides with the TDC of the propeller. From the figure it can be seen that for decreasing radii the velocity trough becomes less steep.

From these inflow velocities and the known rotational velocity of the propeller, which is defined in equation (3.4), the angle of the flow relative to the plane of rotation of the propeller can be calculated from which the geometrical angle of attack can be derived (equation (3.5). The results are plotted in figure 3.9.

Since the inflow velocity reduces towards the wake generator, this results in a decrease of the inflow angle, so closer to the plane of rotation. This in term causes a larger geometrical angle of attack. Where the geometrical angle of attack is calculated according to equation (3.5) where θ is the sectional pitch angle of the propeller blade and α the inflow angle. Because the lift produced is related to the angle of attack via $2\pi\alpha$, an increase in angle also causes an increase of the lift production. Whether the propeller blade remains in its linear lift regime is difficult to say since this is influenced by both the induced velocity and the zero-lift angle of the section of the propeller blade. According to Anderson [1991] the zero-lift angle, $\alpha_{L=0}$, for thin cambered airfoils can be calculated with equation (3.6) which results in an angle of $\alpha_{L=0} = -2.98$ and is constant over the radius of the propeller. The induced velocity can however not be calculated this easily. Since this is outside the scope of this research, no further effort in finding this value is put in.

$$V_p = 2\pi f R \tag{3.4}$$

$$\alpha_g = \theta - \alpha \tag{3.5}$$

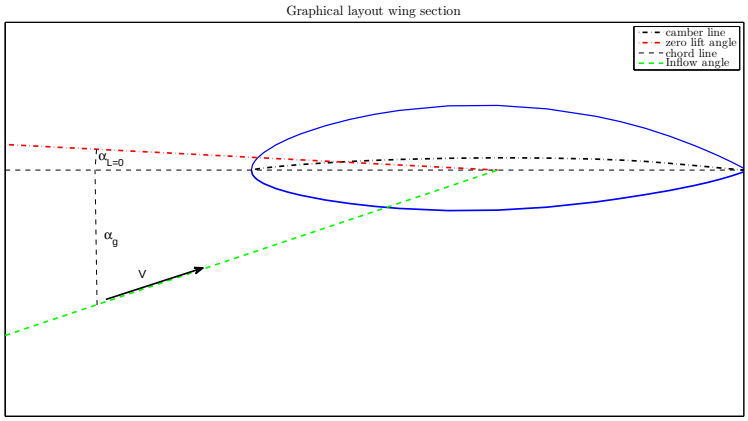

Figure 3.10: Graphical description of wing related terminology

$$\alpha_{L=0} = -\frac{1}{\pi}\int_0^{\pi}\frac{dz}{dx}(cos\,\theta - 1)d\theta \tag{3.6}$$

3.4.2. SPECTRAL ANALYSIS

In 3.1 it was already indicated that the sharpness of the wake was related to the possibility of tip-vortex excitation. The more the waveform encountered by the propeller looks like a rectangular block wave, the more frequencies it can excite. This relation can be shown by a Fourier transform of the block wave shape. For the waveforms of both the dimensionless velocity as the geometrical angle of attack a spectral analysis has been made of which the results are shown in figure 3.11.

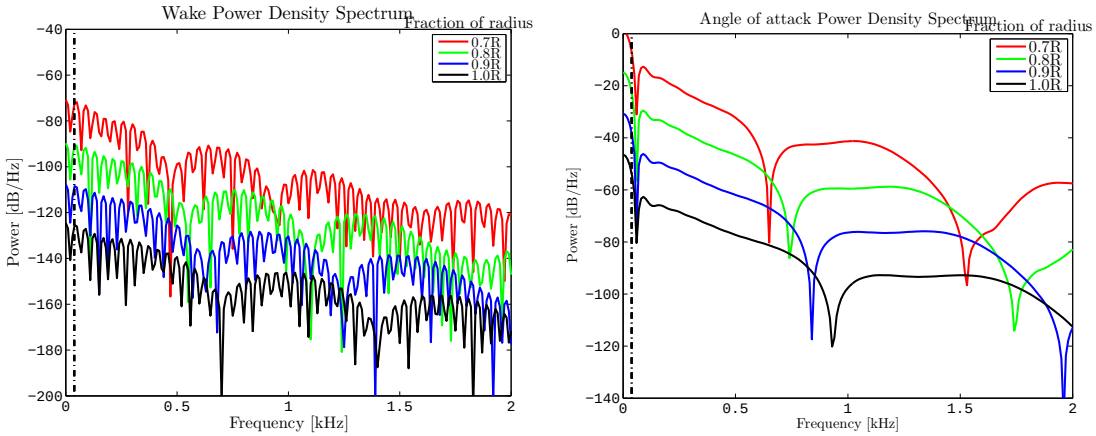

(a) Inflow Velocity PSD in $[\frac{(m/s)^2}{Hz}]$

(b) Angle of Attack PSD in $[\frac{\alpha^2}{Hz}]$

Figure 3.11: Power Spectral Density of the inflow velocity and the angle of attack. In the figures the lines for 0.7R are in the original place. The other lines are all given a successive -15dB offset for presentation purposes

In the figures the line of 0.7R are in the correct place. Each successive radius has an offset of -15dB from the previous one for presentation purposes. From the figures it is evident that, except for perhaps the propeller frequency of 38 Hz, there is no clear power peak in the spectrum. It does appear that for smaller radii the spectrum leans more towards the lower frequencies which correlates to the earlier found less pronounced block wave shape for these radii (see figure 3.9).

The excitation of the tip-vortex cavity most likely occurs due to a sudden large change in the strenght of the tip-vortex. This strength is strongly related to the integrated blade circulation which in turn is strongly related to the angle of attack. Therefore the spectral behaviour of the angle of attack, as shown in figure 3.11b, is probably the most indicative of the spectral behaviour of the cavity.

SEIUN MARU

To see whether the artificial wake is also representative for a real case wake, the wake velocities and the resulting PSD for the Seiun Maru vessel are plotted as sown in figure 3.12. From this it can be seen that both the dimensionless encountered flow velocity and the behaviour of the spectral density is comparable to the graphs that apply to the tunnel test as shown in 3.11a and figure 3.9a. Because the wake of the Seiun Maru is slightly smoother, the peak amplitudes of the PSD tend to be towards the lower range of the frequency spectrum.

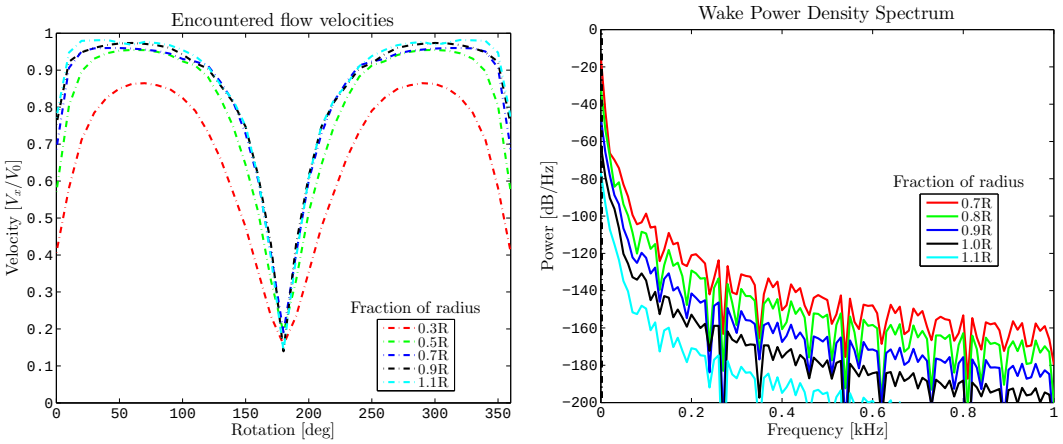

(a) Encountered wake Seiun Maru

(b) Wake PSD in $[\frac{(m/s)^2}{Hz}]$

Figure 3.12: Encountered inflow velocity and wake PSD of the Seiun Maru. In the right hand figure the lines for 0.7R are in the original place. The other lines are all given a successive -15dB offset for presentation purposes

4

NUMERICAL SIMULATION

For the center frequency of tip-vortex cavitation to be predicted, the cavity radius and the azimuthal velocity at the cavity radius must be known as was previously presented in chapter 2. Because a propeller constantly rotates it is difficult to make accurate velocity measurement of the rotational velocity of the tip-vortex, therefore a numerical simulation of the propeller will be made in order to find the cavity radius and the associated circumferential velocity. This chapter focusses on the set-up and the results of these simulations.

4.1. SIMULATION SET-UP

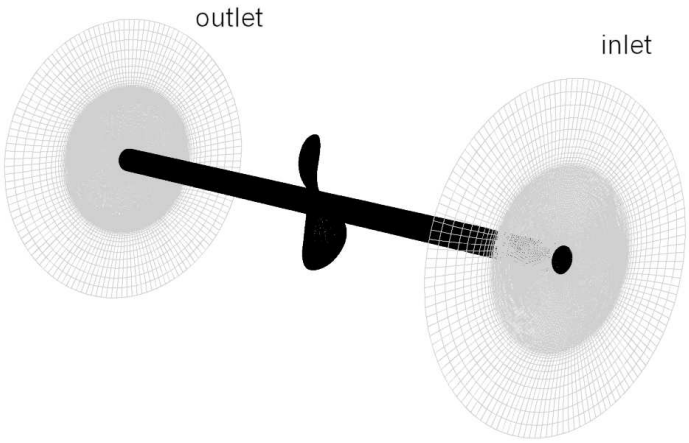

Figure 4.1: Schematic view of the calculation domain setup.

4.1.1. THE GRID

For the simulation a fully structured grid produced with GridPro 3D by MARIN is used. The size of the domain is related to the dimension of the cavitation tunnel resulting in a diameter of 0.34 m which is $2.3D$ and the length of the domain is 0.75 m or $5D$ and is symmetrically positioned relative to the rotation plane of the propeller. The diameter of the domain is chosen such that the surface through which the water flows is equal to the surface of the cavitation tunnel. The 2-bladed propeller, as was used by Pennings [2016], is created with the same file as was used for propeller production and is therefore considered accurate. Although the propeller shaft is finite in the tunnel measurements, to prevent numerical instabilities at the sudden ending of the propeller shaft, it is modelled continuous throughout the domain. The model is oriented along the x-axis where the positive x-axis points into the flow.

In the grid generation, the cells on the propeller blade are given a y^+ value on the order of 1 and it should be smaller than 10 for the linear behaviour in the viscous sub layer to be applied. That this is the case for all three grids used for these calculations is shown in figure 4.2 where can be seen that it has maximum values

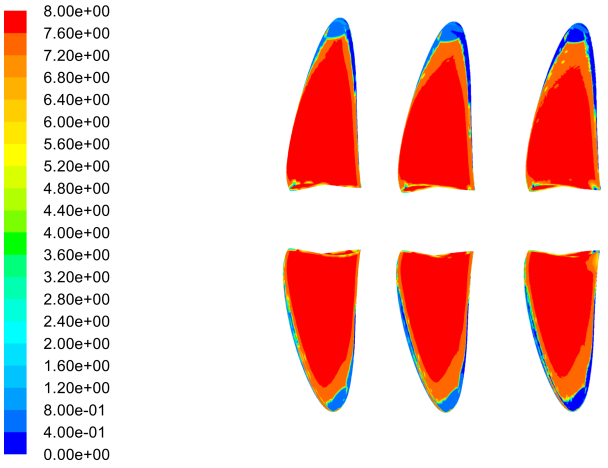

Figure 4.2: From left to right: y^+ values of 0.64 grid, 0.80 grid and 1.0 grid.

of about eight. The influence of the shafts velocity shear on the cavitation behaviour is considered to be insignificant and therefore the cell height on the shaft is not dimensioned to a certain $y+$ value. Because of this, the boundary condition of the shaft is handled differently which will be discussed in the next section.

4.1.2. NUMERICAL SET-UP

For the simulation of the cavitation behaviour Ansys Fluent 15.0 is used. This program is chosen because it incorporates the Spalart-Allmaras one equation turbulence modelling scheme. Also the strain/vorticity correction and curvature correction terms that can be used with this model are already present in the program. These corrections are used for vortical flows and ensure that vortical structures, such as a tip-vortex, are dissipated more slowly. The applicability of the Spalart-Allmaras model, with inclusion of the correction terms, to the simulation of a cavitating tip-vortex was shown by Schot et al. [2014].

A steady-state calculation is performed with boundary conditions of the computation model set up as follows. To incorporate the rotation of the propeller a frame motion around the positive x-axis of 38 Hz or 238.76 rad/s is applied to the model. This ensures the reference frame and geometry stay aligned whilst a rotational velocity is applied to the propeller and shaft. Another factor that is important in the boundary condition settings of the blades and propeller shaft is the slip conditions. For the propeller blades a no-slip boundary condition is adopted whereas for the shaft a slip condition with zero shear is chosen. This makes the earlier choice of near-wall cell height feasible.

On the inflow side of the domain a constant flow velocity of 3.2 m/s is prescribed which is consistent with tunnel measurement for $J = 0.56$. The outflow boundary condition is chosen to be a pressure condition since this does not prescribe any restriction on the outflow in terms of fluxes and gradients. The boundary condition for the outer wall is set to symmetry which ensures that no normal velocities are present and that all flow variables have a zero normal gradient at the wall. Finally a single phase flow simulation is performed.

ENCOUNTERED DIFFICULTIES

From initial calculation it was found that the complexity of the flow causes convergence problems when a segregated solver was used, in this case the SIMPLE scheme. The lack of converge was already clearly visible in the thrust and torque produced by the propeller and the calculation were therefore discarded. With a more robust, yet slower, solver the convergence was good as can be seen from table 4.2. The solver that was used for these calculations was Fluent's COUPLED scheme. To aid the convergence of the solution all spatial variables are discretized using a second-order discretization. Furthermore the standard settings for the relaxation of the pressure and momentum are slightly decreased to further improve the convergence of the solution.

The reason initially the SIMPLE scheme was used, is that it is a much faster method than the COUPLED scheme and is the advised solver, however it was found out that the use of the coupled pressure-velocity scheme gives a much more robust solution, especially when large gradients are present in the flowfield and thus significant changes can occur while going from solving the momentum equations to the pressure equations and vice versa in the segregated solver.

4.2. RESULTS

In this section the results of the numerical simulations, with the settings as presented above, will be discussed. Firstly, the validity of the numerical simulation will be presented and secondly, the results in terms of cavity properties will be presented and verified.

For the analysis three similar grids with each a different level of refinement throughout the domain are used. The grids shall be referred to as the 0.64, 0.80 and 1 grid where the number denotes the fraction of the cell edge length resulting in the numbers of cells as presented in table 4.1.

Grid	0.64	0.80	1.0
N_o Cells [Million]	2.38	5.37	10.5

Table 4.1: Number of cells per grid.

4.2.1. VERIFICATION

The verification of the numerical simulation is focused around the principle of *solving-the-equations-right*. It is performed to check whether the chosen mathematical modelling is correct and the discretized model is solved correctly. To this end, a look is taken at the numerical error of the solution and its convergence. The numerical error is made-up of the round-off error which is the result of the finite accuracy of the computer, the iterative error which is the result of the mathematical modelling of the flow and finally the discretization error. The contribution of the round-off error to the numerical error tends to increase with increasing grid size whereas the contribution of the discretization error shows an opposite trend.

For the calculations made the L_1 and L_∞ norm are used as an indication of the numerical error. The L_1 norm gives the average error over the domain and the L_∞ gives the maximum error in the domain. Both definition are used to obtain insight in the behaviour of the model throughout the domain. The small values of the L_1 norm shown in table 4.2 indicate that the error in global mass and momentum conservation are very small. The larger values of the L_∞ norm show that locally there are higher errors in the flow. Further investigation shows that these larger errors are located in the direct vicinity of the propeller and its associated tip-vortices which is to be expected.

Norm	ΔP	Δm	Δu	Δv	Δw
L_1	10^{-12}	10^{-13}	10^{-10}	10^{-11}	10^{-11}
L_∞	10^{-7}	10^{-9}	10^{-6}	10^{-6}	10^{-6}

Table 4.2: Order of magnitude of residual data of L_1 and L_∞ norm.

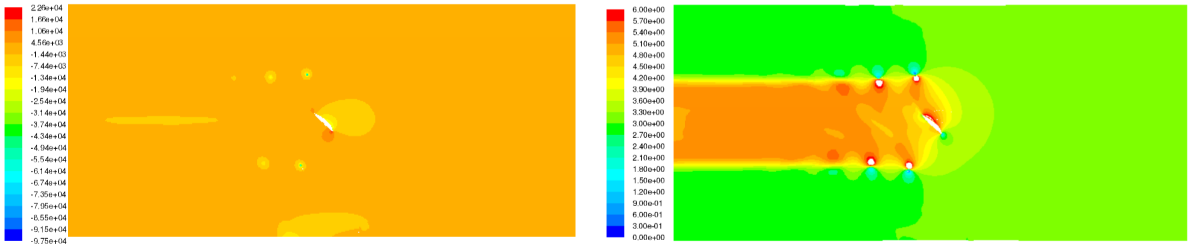

(a) Static Pressure [Pa]

(b) Velocity Magnitude $[m/s]$

Figure 4.3: Plots of static pressure and velocity magnitude along the x-axis. Flow direction is from right to left.

From figure 4.3 it can be seen that no sudden pressure or velocity changes at the inflow and the outflow are present and thus the application of the boundary conditions is considered accurate for this calculation. From a detailed view of the inflow and outflow conditions it can be seen that small perturbations in both pressure and velocity are present as indicated in figures 4.4 and 4.5. There is a clear saw-tooth like pattern visible in both the plots of the pressure and the velocity. These perturbation are present throughout the domain and only appear at the outside wall. Since these perturbations are of a small magnitude relative to the pressures

around the propeller, they are considered to have no significant influence on the cavitation behaviour. The cause of these perturbations will be handled in section 4.3.

From the above data it is concluded that the simulation has proper convergence towards a steady state solution and that at this steady state the maximum numerical error is sufficiently small. Also the size of the domain is sufficient to ensure smooth inflow and outflow conditions at the boundaries without any significant pressure or velocity jumps. So the calculation indeed appears to be able to *solve the equations right.*

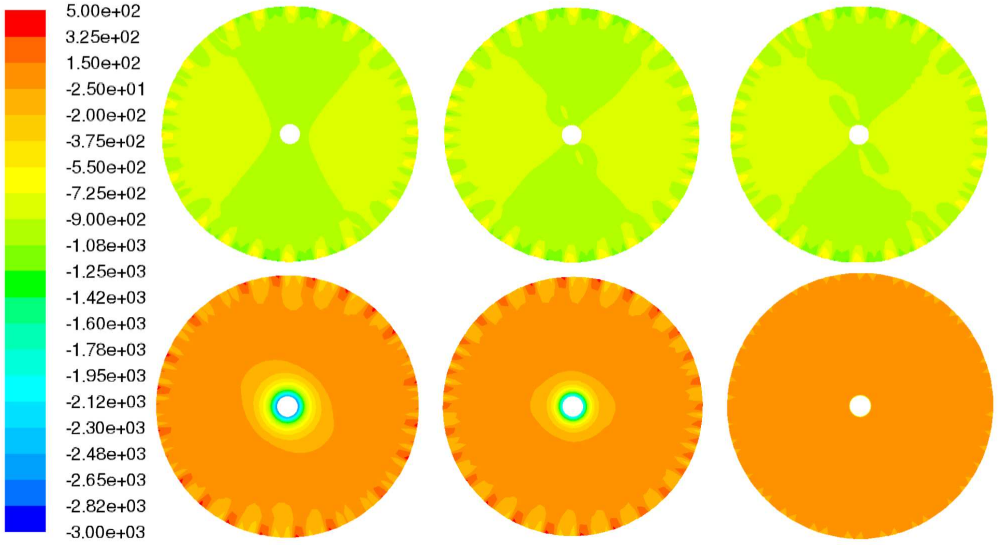

Figure 4.4: Plots of static pressure near inflow (top) and outflow (bottom) at, form left to right, 75mm, 25mm and 0mm ahead of the prescribed boundary. The pressure values are relative to a zero ambient pressure. [Pa]

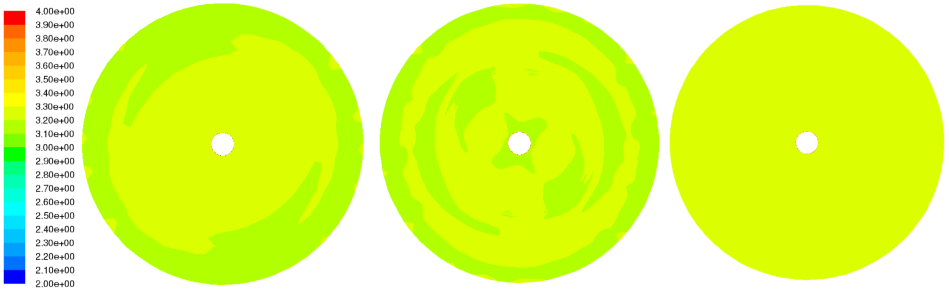

(a) Inflow velocity

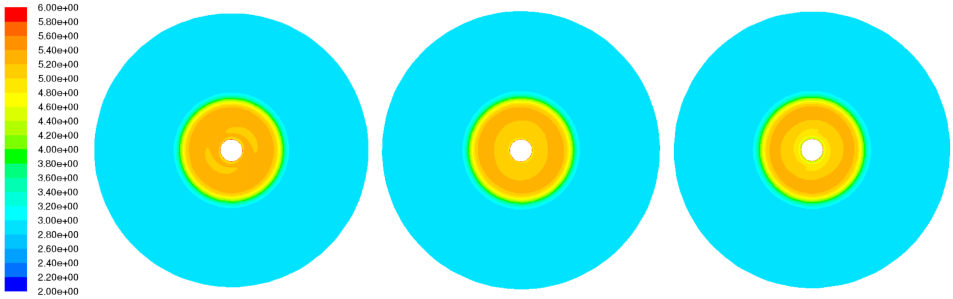

(b) Outflow velocity

Figure 4.5: Plots of velocity magnitude near inflow (top) and outflow (bottom) at, form left to right, 75mm, 25mm and 0mm ahead of the prescribed boundary. [m/s]

4.2.2. INITIAL VALIDATION

From the previous section it was found that the simulation generates mathematically accurate results. In this section it will be considered whether these results also give the answers to the right questions, thus *solving the right equations*. The strength of the tip-vortex is closely related to the strength of the circulation of the propeller blade with which the production of lift is associated. Therefore, as a check on the validity of the numerical settings, the overall quantities of thrust and torque produced by the propeller will be compared to the experimental data presented by Pennings [2016], as shown in table 4.3.

	Measurement	0.64	0.80	1
Kt	0.173-0.176	0.1771	0.1789	0.1803
10Kq	0.267-0.274	0.2446	0.2459	0.2472

Table 4.3: Validation data Kt & Kq.

It can be seen in the table that measurement data and calculated data for the three grids show good agreement although the values of the torque coefficient, Kq are slightly lower for the numerically simulated cases. Furthermore, a clear increase in the thrust coefficient and torque coefficient for increasingly refined grid can be observed. This behaviour is in itself very normal since increased fineness of a grid should give more accurate results. However, since there is no analytic solution to the problem there is no definitive value towards which the numerical simulation should converge. A convergence study with increasingly fine grids to find a converged solution can be performed, but this is outside the scope of this thesis.

Since the values of the calculated torque coefficient and the thrust coefficient are close to their measured counterparts, it can be concluded that the propeller blade loading is modelled accurately in the numerical simulation. Since the tip-vortex is a result of the blade loading, it is assumed that the vortex strength is also calculated correctly and that the computations can be used to get insight in the cavitation behaviour of the tip-vortex.

4.2.3. MESH REFINEMENT

The mesh, as it is generated by MARIN, is capable of calculating the general behaviour and parameters that are associated with propellers, such as thrust and torque, it is however not able to keep vortical structures in existence. This is due to the relative coarseness of the grid compared to the diameter of the vortex core.

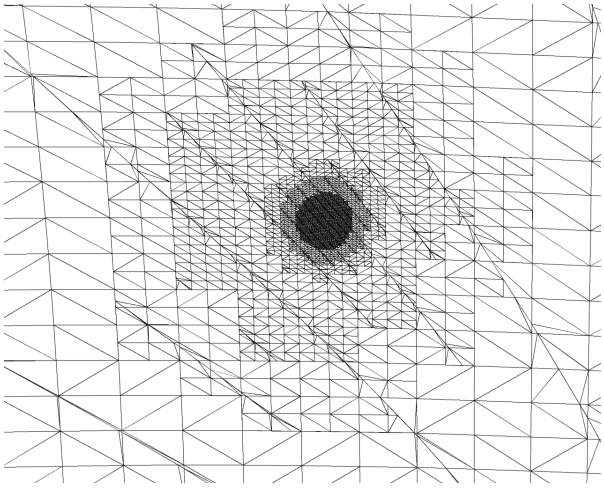

Figure 4.6: View of the stepwise-increased mesh refinement at the vortex core.

To capture the low pressure vortex core that is associated with vortex cavitation, a scheme of successive mesh refinements is chosen. This scheme consist of a refinement of the mesh based on the static pressure of an initial converged solution of the simulation. The refinement iterations are based on consecutively increasing numbers of the surrounding pressure p_∞. Based on this value a region from zero to the indicated surrounding pressure will be selected for refinement. For small values of p_∞ a relatively large part of the

computational domain will be selected. To prevent a sudden large decrease of cell size in the domain, which might cause computational errors, along with the increase of the surrounding pressure the cell volume will be decreased. This causes the domain around the vortex to have an increasing level of refinement towards the vortex core. The final step in the refinement has a cell volume of $1.221 * 10^{-13}\ m^3$ which results in a cell edge length of about 0.05 mm. This value is chosen to get a sufficient degree of refinement within the vortex core to be able to capture the high pressure gradients and velocity gradients.
When all steps of one refinement iteration have been performed, the simulation is run again until a converged solution is obtained upon which the next refinement iteration can be performed.

From figure 4.7 it can be seen that the number of cells quickly increase with each refinement iteration. The initial mesh sizes for the 0.64, the 0.80 and 1 grid are 2.4 million, 5.4 million and 10.5 million cells respectively. So although the multiplication during the second refinement of the 1.0 grid is only 1.4, this does mean an increase of 4 million cells in a very small region of the domain. Since this large increase is mainly caused by the refinement steps with the smallest minimum volumes, the regions that this is applied to is chosen as small as possible whilst maintaining a sufficient refinement in the vortex core. The resulting grid sizes for each of the starting grids is shown in table 4.4.

Grid	0.64	0.80	1.0
N_o Cells start	2.38	5.37	10.5
N_o Cells end	12.9	11.4	14.7
N_o Refinements	9	4	2

Table 4.4: Number of cells, in millions,per grid before and after all refinement iterations.

In the process of refining the grids, it was found that it is better to perform more steps per iteration instead of few large steps. Another aspect of the refinement steps is the possibility to create degenerate cells and/or inverse surfaces. To prevent this, each successive minimum cell volume is decreased with a factor of a multiple of two.

4.2.4. CAVITY DATA

In this section the effect of successive refinement iterations on the azimuthal velocity and the cavity radius will be presented. Next, the influence of the numerical dissipation on the cavity parameters is reported. Finally, the resulting cavity size will be compared to the measurement data as presented by Pennings [2016] which serves as a further validation of the calculation model.

The different grids have undergone different refinement steps as well as a different amount of iterations. It can be imagined that a coarser grid, such as the 0.64 grid, needs more refinement steps to generate a vortical structure with a certain length than a finer grid. The refinement steps undergone by the 0.64 grid and the effect on its number of cells is shown in figure 4.7.

Since a single phase flow is simulated, there is no real cavity present in the calculation. Therefore the size of the cavity is defined as the position at which vapour pressure occurs in the flow. This way a wetted vortex is

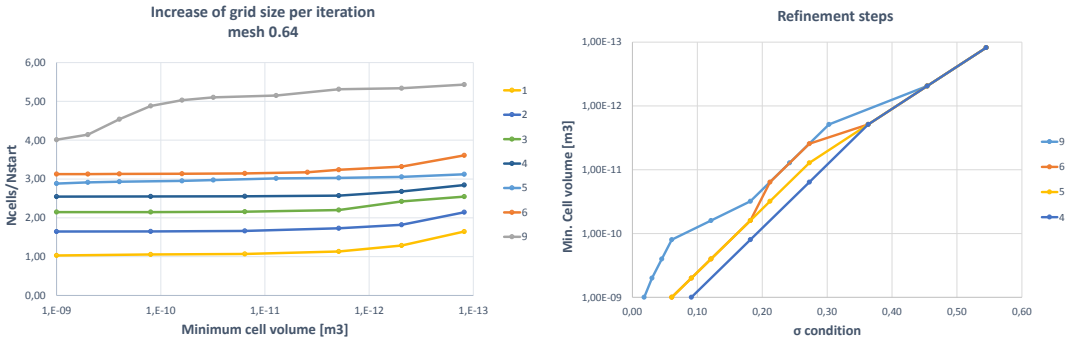

Figure 4.7: Steps of the mesh refinement process. Nstart is the number of cells of the original mesh. σ indicates the cavitation number of the outer pressure boundary. The lines indicate the refinement steps taken in one iteration.

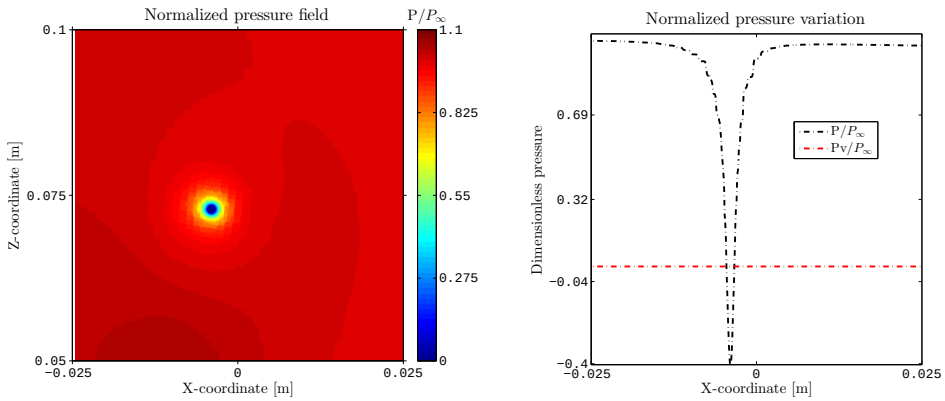

(a) Pressure field

(b) pressure through vortex core

Figure 4.8: Left:Plot of normalized pressure field on the plane perpendicular to the vortex tube. Right: Pressure distribution over x-axis through the vortex core. Plots are for a condition of $\sigma \approx 0.55$ and show the pressure field of the 0.80 grid after the third refinement iteration at the point 0.8*chord behind the tip.

used to define the cavity radius and the azimuthal velocity of the vortex which was shown by Bosschers [2010] to give good agreement to actual cavitation conditions.

The pressure field data of the numerical simulation is exported from a plane perpendicular to the vortex tube. This plane is positioned at a distance of 0.8 times the blade chord at 0.7R behind the tip of the propeller and has dimensions of $50 * 50\ mm$. This position is chosen because it was also used in the measurements conducted by Pennings [2016] and thus reference data is available. A typical view of the pressure data on this plane as well as a pressure distribution over the x-axis through the core of the vortex are displayed in figure 4.8. The pressure data is normalized with the surrounding pressure P_∞. In appendix A plots of all grids after their final refinement iteration can be found.

figure 4.8b shows a clear deep and steep pressure through which is coherent with expectations. In the figure the red line indicates the dimensionless vapour pressure at which the cavity radius is determined. The intersection of the two lines indicates the radius of the cavity.

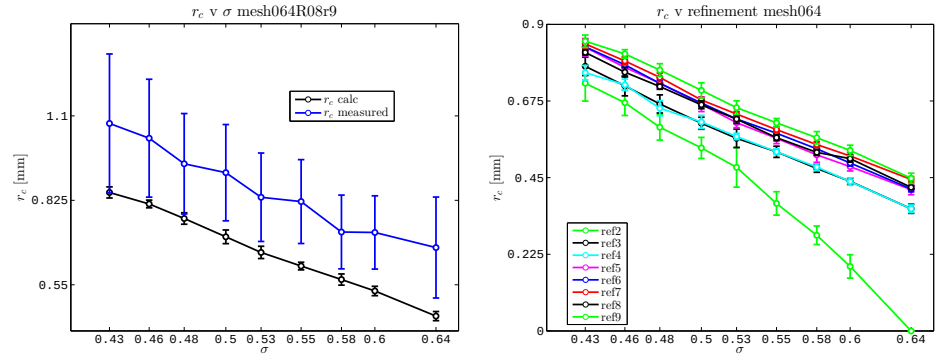

(a) 0.64 Grid after the final refinement iteration. (b) 0.64 Grid for refinement steps as indicated in figure 4.7.

Figure 4.9: Mean and standard deviation of the calculated and measured cavity radius for different values of the cavitation number σ and the effect of refinement iterations on the cavity size. Data is from the plane 0.8*chord behind the tip of the propeller blade.

Through finding the location of this intersection over the full circumference of the vortex core and calculating its distance from the center of the vortex core, the mean radius can be found as is shown in figure 4.9a. Here it can be seen that the trend of the calculated cavity radius as function of the cavity number compares quite well to the measured radii. It is also clear that the calculated value of the cavity radius is well below the measured values. Therefore a check of the convergence of the cavity radius as function of the refinement iterations is performed. The results for the 0.64 grid of this convergence study is shown in figure 4.9b. The 0.64 grid is chosen for this since it has undergone the most refinement steps and thus should give the best insight

into the converging behaviour. In this figure the effects of the first and second refinement are not shown since they did not yet lead to pressures below vapour pressure in the vortex core and thus no cavity radius could be defined.

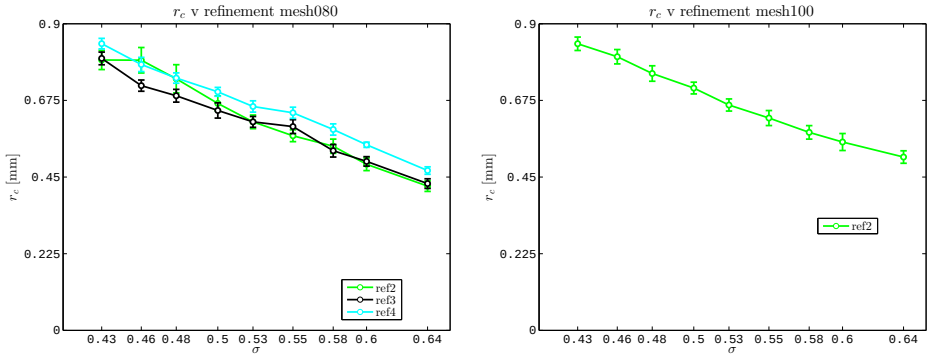

(a) Grid 0.8 (b) Grid 1

Figure 4.10: Mean and standard deviation of the calculated cavity radius as function of the cavitation number σ for different refinement iterations.

From figure 4.9b it can be seen that the cavity size does grow in diameter with each iteration step, however this paints a somewhat simplified picture, namely, not all refinement iterations contain the same steps. For the 0.64 grid the first four refinement iteration use the same pressure levels and minimum cell volume values. Looking at the effect of the fourth refinement iteration, it can be seen that the cavity radii are nearly the same and thus, at least for the plane that is looked at, it has hardly any influence on the results. The refinement iteration does however cause the cavity to grow in length and thus there the smaller cells are generated.

Because of this notion a new refinement scheme was used for iterations 5 and 6, as can be seen in figure 4.7, which consisted of smaller cell volumes at a higher pressure condition. This ensures a refinement further from the vortex core and clearly also causes an increase in the cavity size. However, this too appears only to work for one refinement iteration since the sixth refinement step again produces very similar cavity sizes as were found after the fifth iteration. So it appears that the refinements away from the vortex core have a large influence on the cavity radius itself, which would mean that the denser grids of 0.8 and 1.0 should produce larger cavities. To see if the increase of the range improves the results, iterations 7 and 9 are performed where for iteration 7 the range of the refinements is moderately increased and for iteration 9 the range is chosen as large as practically possible with the current range selection criterion. To check if further refinement of the core improves the prediction of the cavity diameter iteration 8 is performed. Iteration 7 and 8 show only very small improvements, iteration 9 however shows a significant increase of the cavity radii.

As can be seen in figure 4.10, where the effect of the refinement steps on the cavity radii for the 0.8 grid and 1 grid are shown, the finer grid surrounding the cavity indeed appears to improve the prediction of the cavitation radius as was also found for the last refinement iteration of the 0.64 grid. The refinement steps taken in the last iteration of both grids are the same as the last two steps for the 0.64 grid. The omitted refinement iteration did not generate pressures below vapour pressure. For the 0.8 grid it can be seen that here too the cavity size does not significantly increase from the second to the third refinement step.

For the azimuthal velocity the same trend can be observed for the increase with refinement as well as the grid dependency as is presented in figure 4.11. Also, as was the case for the radii, the refinement steps containing the same refinement pressure levels and minimum cell volumes, do not further increase the values of the azimuthal velocity after a few iterations.

The validity of the calculated results and its applicability to the calculation of the center frequency of the cavitating vortex will be presented in the next section.

CHORD WISE DECAY

In section 4.1.2 it was mentioned that the choice of the Spalart-Allmaras turbulence model with inclusion of correction terms was chosen because of its capability to maintain vortical structures further downstream. From experiment it can be seen that almost regardless of the cavitation number the propeller performs at, the cavity remains visible far downstream as can be seen in figure 4.12. That this is not the case for the numerical

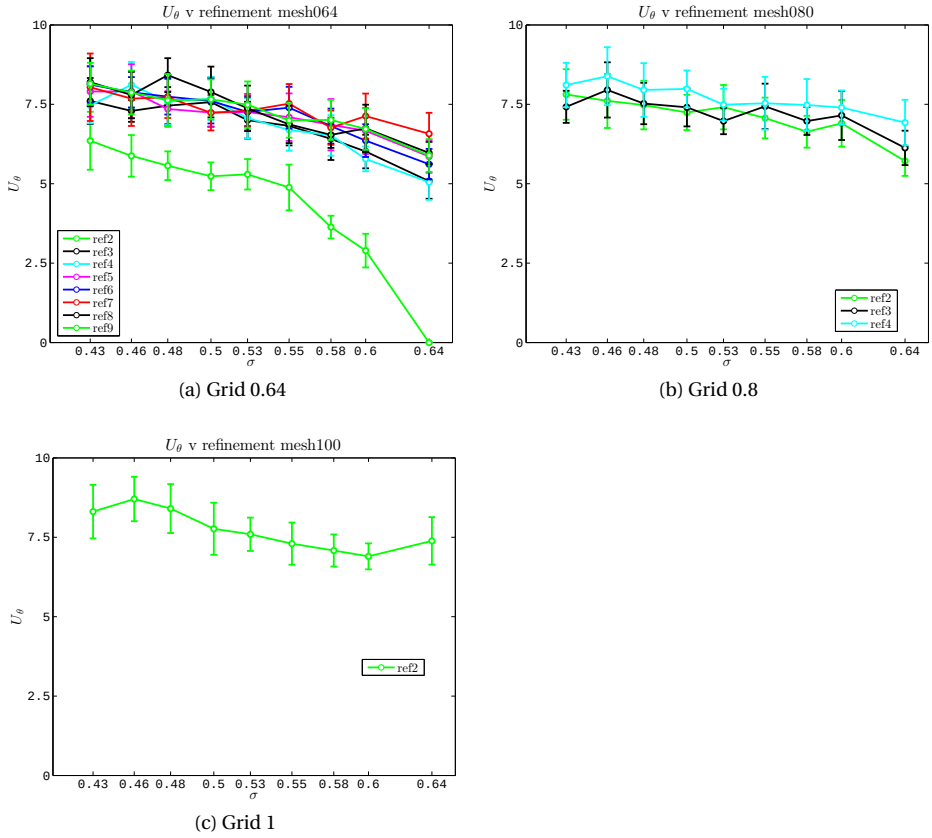

(a) Grid 0.64

(b) Grid 0.8

(c) Grid 1

Figure 4.11: Mean and standard deviation of in-plane azimuthal velocity as function of the cavitation number σ for different refinement iterations.

simulation can be seen from figure 4.13 where it is apparent that the cavity only remains present for less than half a rotation, so clearly there still is some non-physical dissipation present.

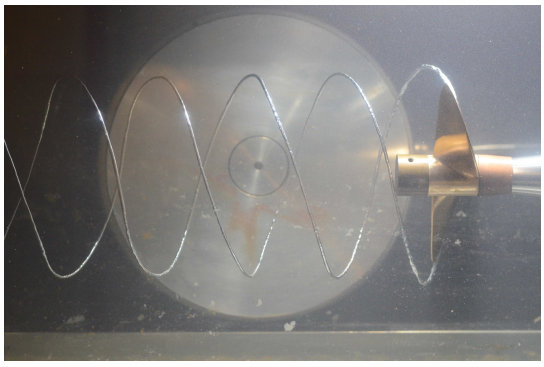

Figure 4.12: Downstream propagation of tip vortex cavity at J=0.56, σ=0.37.

The decay rate of both the cavity radius and the tangential velocity as function of the distance from the tip is therefore investigated. To this end, for the planes of 0.4, 0.6, 0.8 and 1 chord length from the tip, both radius and velocity are calculated as shown in figure 4.14. For values closer to the tip, the propeller blade is still present in the section due to which the important parameters can not be calculated with sufficient confidence.

From these figures it is evident that a significant decay rate is present for all σ values. It can also be seen that lower σ values have a less distinct decay than the higher values. For the tunnel tests a decay rate of less than the measurement error is found for the range of 0.3c to 1.7c behind the propeller and for the purpose

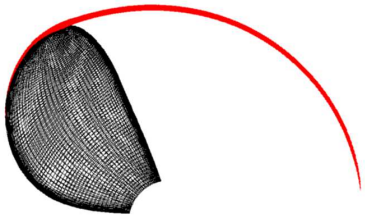

Figure 4.13: Downstream propagation of tip vortex cavity in Fluent at J=0.56. The cavity is the iso-surface of σ=0.37.

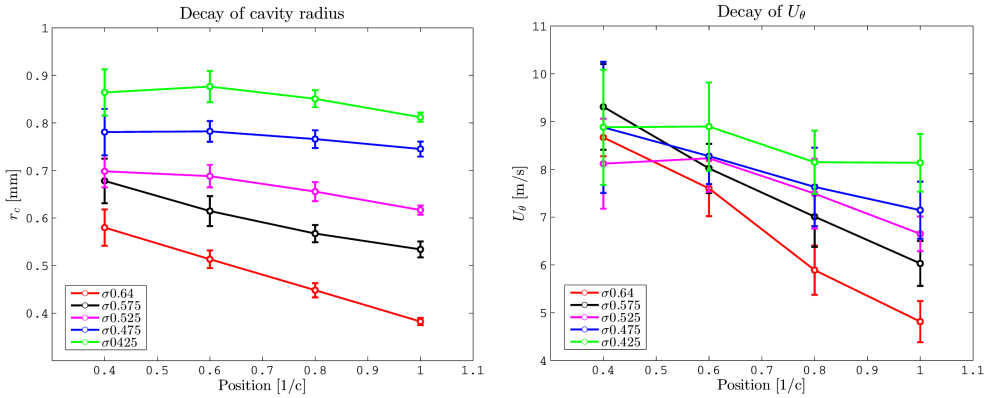

(a) Cavity radius

(b) Tangential Velocity

Figure 4.14: The decay of the cavity radius and the tangential velocity, U_θ, as function of the distance from the tip for several cavity numbers.

of comparison it is considered to be a constant value from just behind the propeller to one chord behind. Because the purpose of these calculations is the accurate prediction of the cavity behaviour and its associated center frequency, the position behind the tip of the propeller that best matches the cavity behaviour from the tunnel tests should be found. This position logically lies closest to the propeller since there the numerical dissipation has the least effect on the cavity properties.

VALIDATION

To check the validity of the calculated cavity data and its resulting sound production, the simulation results are compared to the available measurement data. In the previous section a clear decay rate in the cavity properties was shown. Here the best location to perform a validation of the calculation will be discussed.

From figures 4.15 and 4.16 it can be observed that a decay of the cavity properties is indeed present and also that the plane closest to the propeller, 0.4c, compares best with the measurement data from the tunnel tests as performed by Pennings [2016] as was suggested previously. The calculation of the center frequency is done according to the method described in chapter 2. It can clearly be seen that for all three positions relative to the propeller tip, the cavity radii are smaller than the measured values and that they deviate further from the measured values. The same trend is visible for the center frequency of the sound emitted by the cavity. From this it is concluded that, to prevent or reduce the influence of the numerical dissipation, the plane where the cavity data is calculated should be chosen close to the propeller which in this case is the plane at 0.4c behind the propeller. Here the cavity radius is within the uncertainty range of the measurements for most σ and for all σ values the uncertainty of the measured and calculated radii overlap. The same behaviour is visible for the calculated and measured center frequencies.

The tangential velocity for this plane is shown in figure 4.17 and the change of the tangential velocity with the cavitation number is shown in figure 4.18. Here no reference data is presented because the tangential velocity is nearly impossible to measure in the rotating reference frame of the propeller. Since the tangential velocity is the most influential parameter in the calculation of the center frequency, the accuracy of the calculated center frequencies shown in figures 4.15 and 4.16 suggest that the calculation of the tangential velocity

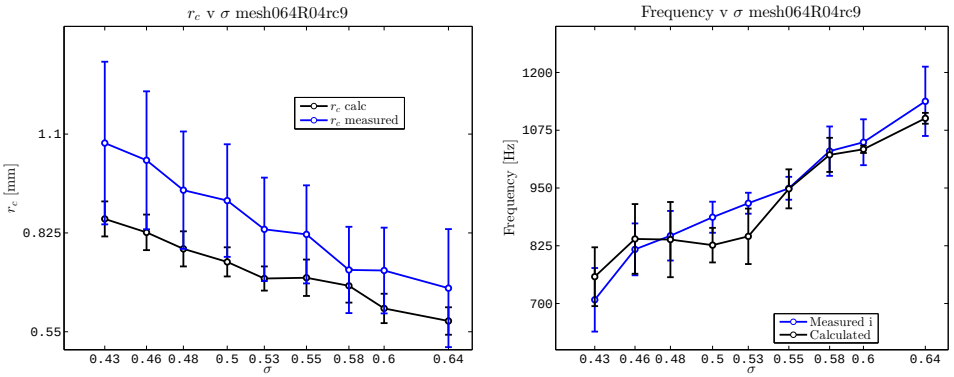

(a) Cavity radius 0.4c

(b) Center frequency 0.4c

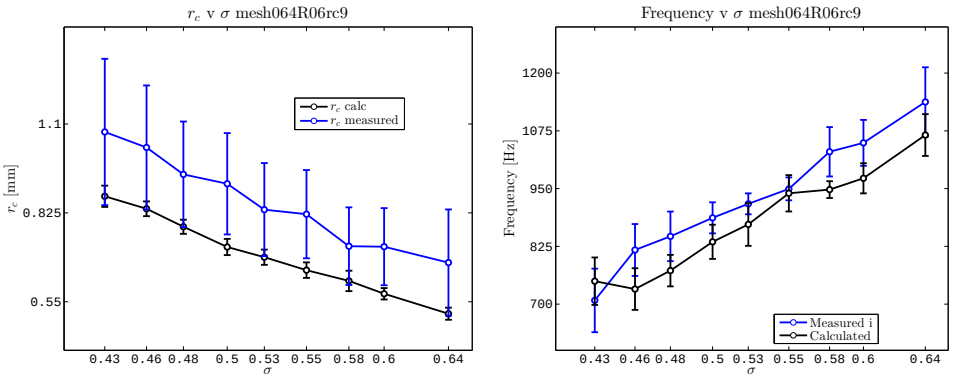

(c) Cavity radius 0.6c

(d) Center frequency 0.6c

Figure 4.15: Cavity radius and resulting center frequency for positions of 0.4 and 0.6*chord behind the tip for the 0.64 grid.

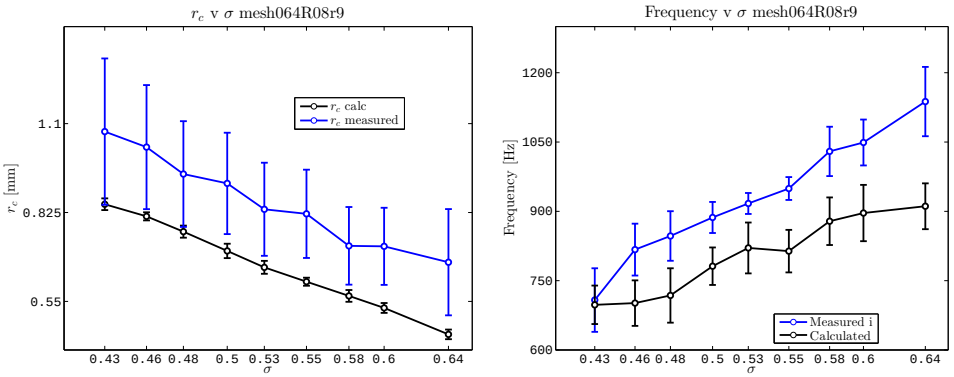

(a) Cavity radius 0.8c

(b) Center frequency 0.8c

Figure 4.16: Cavity radius and resulting center frequency for position 0.8*chord behind the tip for the 0.64 grid.

is also sufficiently accurate.

The dip of the tangential velocity at the point of $\sigma = 0.53$ is probably the result of the calculation method used to define the vortex center. The cause of the large spread for the tangential velocity can be observed in figure 4.17b where the right peak in the tangential velocity is clearly larger than the one on the left. Since the mean tangential velocity is calculated from all points on the edge of the cavity, this results in a large standard deviation and is also the main contributor to the uncertainty in the calculated center frequency.

In figures 4.19 and 4.20 the cavity properties at 0.8 chord behind the tip for the 0.80 and 1 grid are shown.

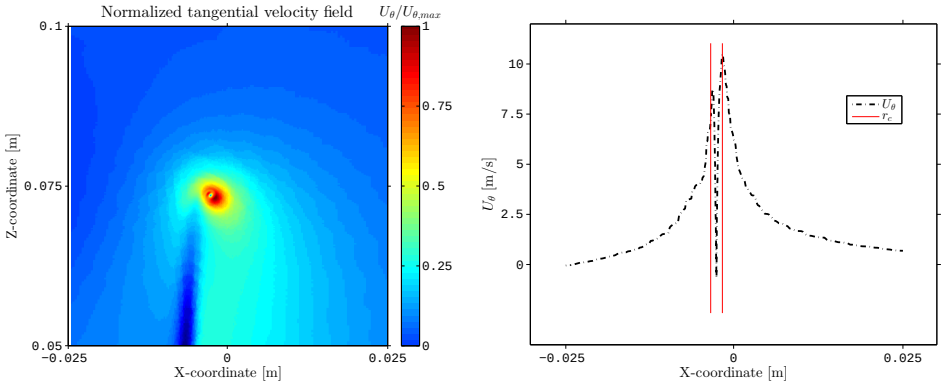

(a) Tangential velocity field (b) Section of U_θ

Figure 4.17: Tangential velocity field and a slice of the velocity field along the x-axis through the core of the vortex at 0.4c and $\sigma = 0.43$.

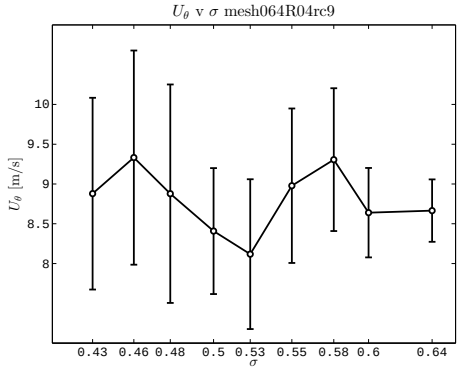

Figure 4.18: Tangential velocity as function of σ at plane 0.4c.

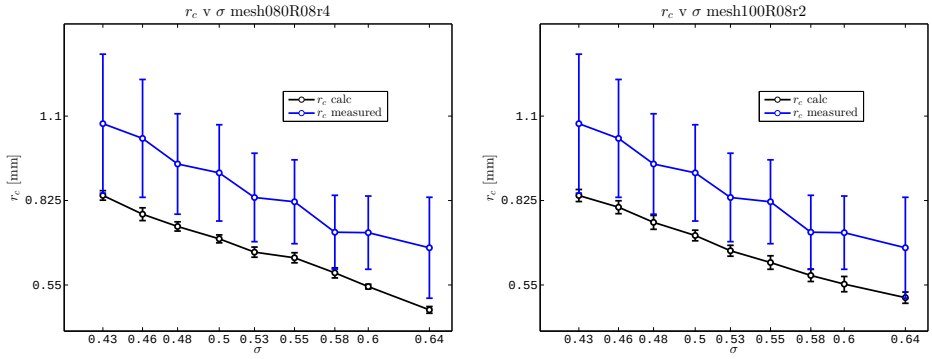

(a) Grid 0.8 (b) Grid 1

Figure 4.19: Comparison of the mean and standard deviation of the measured and calculated cavity radii of grids 0.80 and 1 at location 0.8c.

When this is compared to the results in figure 4.16 it can be seen that the change in cavity radius for the different grids is very small but there is a slight difference in the frequency graph. However, the differences in calculated frequency for all but the $\sigma = 0.64$ condition are within the uncertainty range of the calculated frequency for the 0.64 grid. What can be deduced from this is that the surrounding grid size is not the most important factor in the accurate calculation of the vortex behaviour.

In figure 4.21 the behaviour of the cavity radius, the tangential velocity and the center frequency as function of σ is presented for σ values outside of the measurement scope. The quadratic behaviour of the tangential velocity as it would be expected from the radial momentum equation 2.10 can be seen in figure 4.21b.

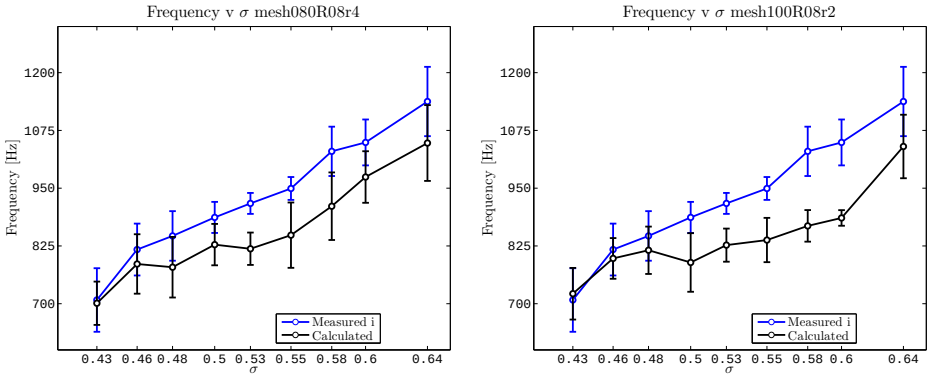

(a) Grid 0.8 (b) Grid 1

Figure 4.20: Comparison of the mean and standard deviation of the measured and calculated center frequency of tip-vortex cavitation for grids 0.80 and 1 at location 0.8c.

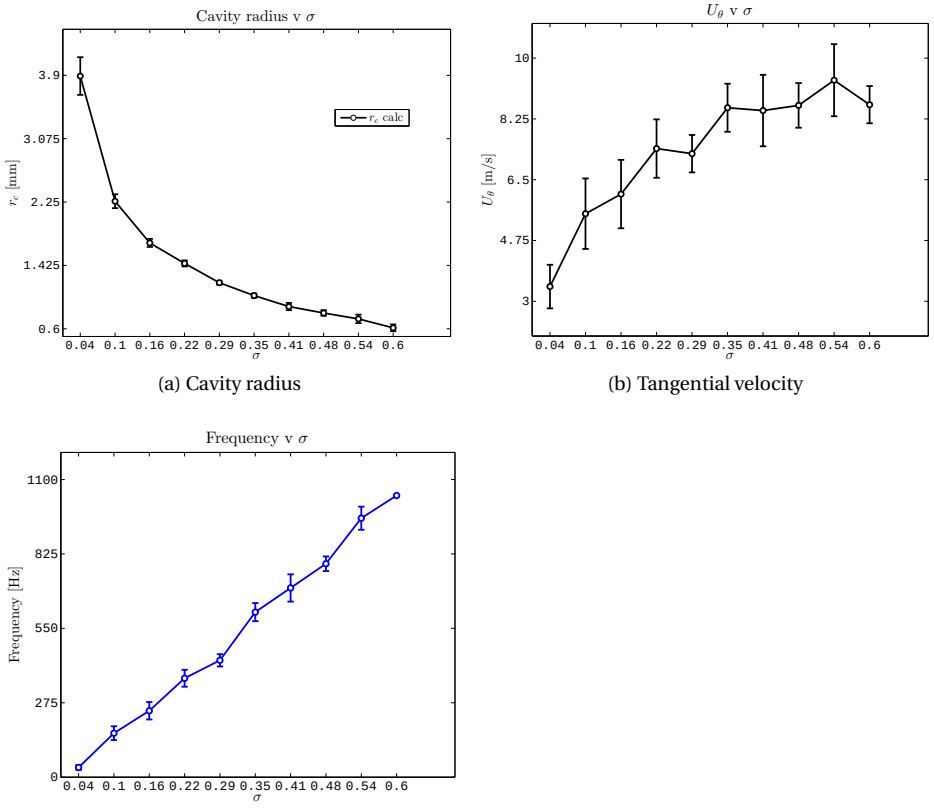

(a) Cavity radius (b) Tangential velocity

(c) Center frequency

Figure 4.21: Plots of the cavity radius, tangential velocity and the resulting center frequency for the 0.4c plane.

4.3. DISCUSSION

In this section, the encountered uncertainties in the numerical simulations as well as the determination of the cavity radius and the circumferential velocity will be handled. Also the significance of the obtained results and the applicability of the methods described in this chapter will be discussed.

During the verification of the numerical simulation, as presented in section 4.2.1, a saw-tooth like pattern of the pressure was found at the outer wall of the domain. Since the pressure perturbations were small these were neglected for the further calculations of the cavitation behaviour. It was found that a potential source of these disturbances was because the outer wall of the domain was not perfectly circular. The variation in radial coordinate of the outer wall and the variation of the static pressure at the wall are shown in figure 4.22. The pressure variation and the variation in radial coordinate clearly show the same saw-tooth like pattern as was observed in figure 4.4. From further research with a simple cylinder meshed with a different mesher, the same behaviour was observed regardless of the boundary and rotation condition that was chosen. For that case the pressure streaks where orientated diagonally along the outer wall. From this it is concluded that the pressure perturbations are not a result of the numerical simulation but are the result of a mesher dependent variation of the outer wall radius.

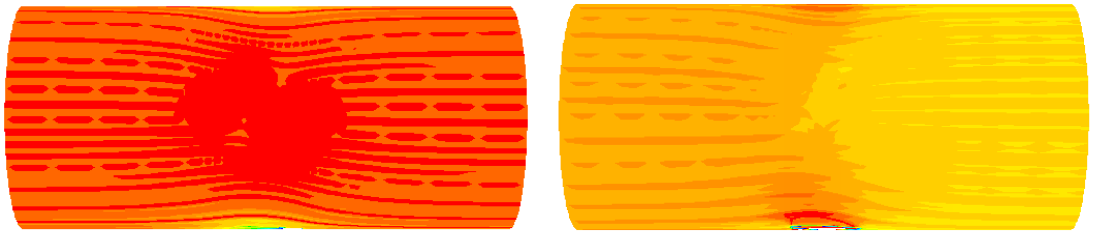

(a) Radial coordinate (b) Static pressure

Figure 4.22: Plots of the variation of the radial coordinate and the variation in static pressure of the outer wall of the domain.

Another aspect of the current calculation method that might be improved is the calculation of the vortex core and the resulting tangential velocity around it. Currently, the core is defined as the point with the lowest pressure as it is exported from Fluent. Since the cavity may not be perfectly round and the plane it is reviewed at might also not be perfectly perpendicular to the vortex core, an error may be introduced there. Furthermore, the velocity profile around the vortex is not axi-symmetric as can be seen from figure 4.17. The deviation of the defined vortex core relative to the real core results in the variation of the tangential velocity as can be observed in figure 4.18. A better definition of the vortex core might further improve the prediction capabilities of the center frequency.

A third point of interest is the interpolation from the unordered grid as it is exported from Fluent to an ordered grid. Currently a cosine spaced grid is used upon which the data from Fluent is interpolated using the eight closest points weighted with $1/r^4$ where r is the radial distance between the point on the ordered grid and the point on the unordered grid. Although this results in grids which are very similar, another number of points or a different method all together might show better agreement.

A last point of interest is the numerical dissipation that causes the non-physical decay of the cavity parameters. Based on the measurement data, it was suggested that the cavity in the tunnel measurements hardly shows any decay and that therefore the location of the plane upon which the cavity data is based can be chosen over a range of chordwise distances. Currently a plane close to the propeller is chosen because here the numerical dissipation has little influence on the cavitation behaviour. Since there is not a range over which the cavity radius and the circumferential velocity is constant, this brings some uncertainty in the choice of location. Further investigation in the reduction of the numerical dissipation, possibly by refinement of the vortex plane coming from the propeller, might result in a more certain choice of the location at which the cavitation behaviour should be evaluated.

With these areas of uncertainty in mind, the method as it is presented is capable of calculating the cavity radius and the circumferential velocity at that radius, resulting in good agreement with the measurement data as produced by Pennings [2016]. Furthermore the center frequency calculated with the dispersion relation

as shown in equation (2.6) using the cavity data from the numerical simulations, agrees very well with the measured sound data. Nevertheless, some areas of the presented method need some further investigation to gain a better insight in the behaviour of the cavity in the simulations and therewith increase the confidence in the choices made.

5

Conclusions & Recommendations

Conclusions

In this thesis the influence of an excitation of a tip-vortex cavity by means of an artificial wake in the cavitation tunnel at the Delft University of Technology is investigated. To investigate the flow variations induced by this wake generator, measurements have been performed from which a steep dip in the flow velocity was found near and behind the wake generator. Also a highly fluctuating behaviour of the flow, with large deviations from the mean flow, was found. These large spreads are associated with the broadband sound spectrum that comes with tip-vortex cavitation and therefore it is concluded that the wake generator as it is used in the measurements by Pennings [2016] gives a good approximation of a real wake.

From the results of the numerical simulations presented in this paper it is concluded that the method described is able to generate results that show good agreement with measurement data. With this method a relatively fast and accurate prediction can be made of the center frequency of tip-vortex cavitation with the use of the engineering method, as presented in chapter 2. However, to grow the confidence in the results produced, further research should be performed.

Recommendations

The current numerical simulations have been performed for a very small propeller. It would be interesting to see whether the method, as it is described and tested here, also produces good results for a regular scale propeller. Next to that, as already mentioned in the discussion of chapter 4, because the cavity shows no chordwise region over which the parameters of interest are constant, a further investigation into the decay rate of the cavity is advised in order to increase confidence in the choice of location at which the cavitation parameters should be evaluated.

BIBLIOGRAPHY

J. D. Anderson. *Fundamentals of Aerodynamics*, volume 5. 1991.

J. Bosschers. Analysis of Inertial Waves on Inviscid Cavitating Vortices in relation to Low-Frequency radiated Noise. In *Proceedings of the Warwick Innovative Manufacturing Research Centre (WIMRC) Cavitation: Turbo-machinery and Medical Applications Forum*, volume 2, Warwick University, United Kingdom, 2008.

J. Bosschers. Investigation of the resonance frequency of a cavitating vortex. In *Proceedings of the NAG/DAGA International Conference on acoustics*, Rotterdam, The Netherlands, 2009a.

J. Bosschers. Investigation of Hull Pressure Fluctuations Generated by Cavitating Vortices. In *Proceedings of the First Symposium on Marine Propulsors*, number June, 2009b.

J. Bosschers. On the influence of viscous effects on 2-D cavitating vortices. *Journal of Hydrodynamics*, 22: 763–770, 2010.

B. Maines and R. Arndt. The Case of the Singing Vortex. *Journal of Fluid Engineering*, 119:271–276, 1997.

V. P. Morozov. Theoretical analysis of the acoustic emission from cavitation line vortices. *Soviet Physics Acoustics*, 19(5):468–471, 1974.

P. C. Pennings. Cavitation tunnel analysis of radiated sound from the resonance of a propeller tip vortex cavity. *Under consideration For International Journal of Multiphase Flow*, 2016.

P. C. Pennings, J. Bosschers, J. Westerweel, and T. J. C. Van Terwisga. Dynamics of Isolated Vortex Cavitation. *Journal of Fluid Mechanics*, 778:288–313, 2015a.

P. C. Pennings, J. Westerweel, and T. J. C. Van Terwisga. Sound signature of propeller tip vortex cavitation. *Unpublished*, 2015b.

P. C. Pennings, J. Westerweel, and T. J. C. Van Terwisga. Flow field measurements around Vortex Cavitation. *Experiments in Fluids*, 56(206), 2015c.

F. H. Proctor. The NASA-Langley Wake Vortex Modelling Effort in Support of an Operational Aircraft Spacing System 36th Aerospace Sciences Meeting & Exhibit January 12-15 , 1998 / Reno Nevada of an Operational Aircraft Spacing System. *Aiaa*, 98-0589, 1998.

J. A. Schot, P. C. Pennings, M. J. B. M. Pourquie, and T. J. C. Van Terwisga. Modelling of Tip Vortex Cavitation for Engineering Applications in Openfoam. (WCCM XI):1–2, 2014.

Sir W. Thomson. Vibrations of a columnar vortex. *Philosophical Magazine Series 5*, 10(61):155–168, 1880.

A

APPENDIX A

This appendix contains the graphs of the velocity, pressure, cavity radius and center frequency for all three grids after their last refinement iteration.

MESH 0.64

VELOCITY

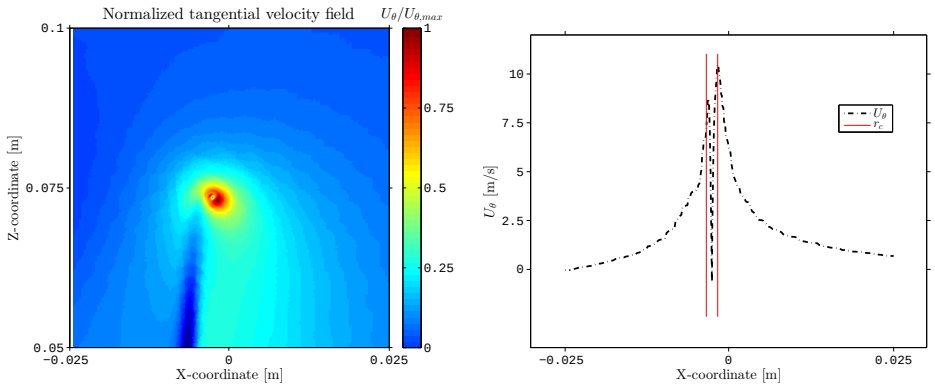

(a) U_θ (b) U_θ through core

Figure A.1: Tangential velocity at 0.4c.

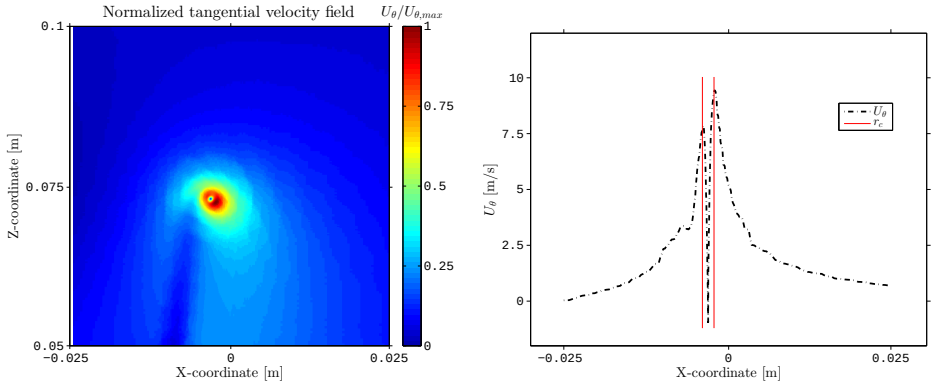

(a) U_θ (b) U_θ through core

Figure A.2: Tangential velocity at 0.6c.

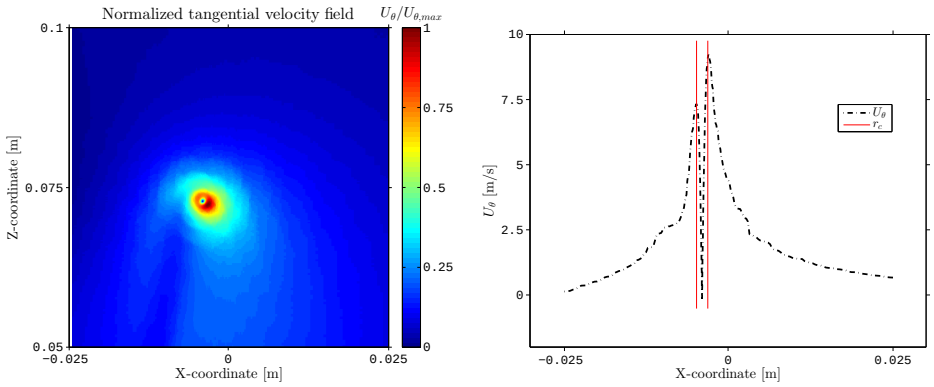

(a) U_θ (b) U_θ through core

Figure A.3: Tangential velocity at 0.8c.

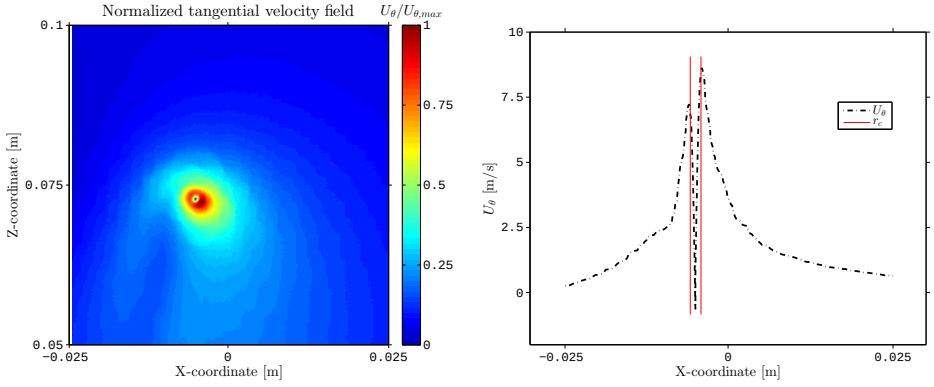

(a) U_θ (b) U_θ through core

Figure A.4: Tangential velocity at 1.0c.

PRESSURE

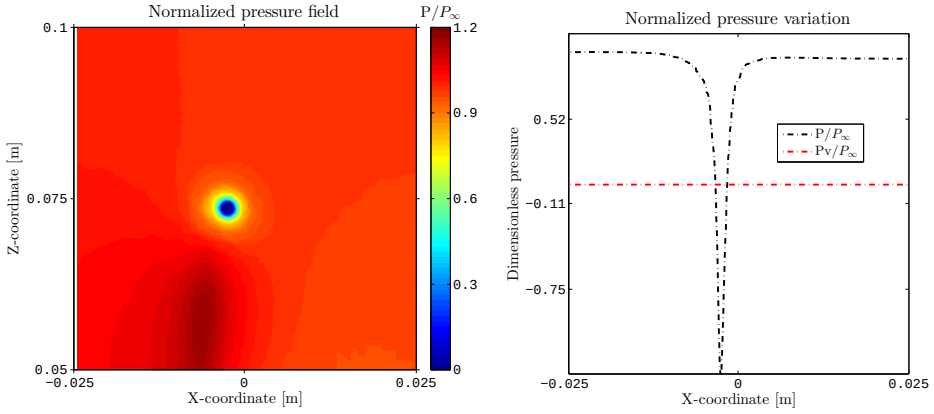

(a) Pressure (b) Pressure through core

Figure A.5: Pressure at 0.4c.

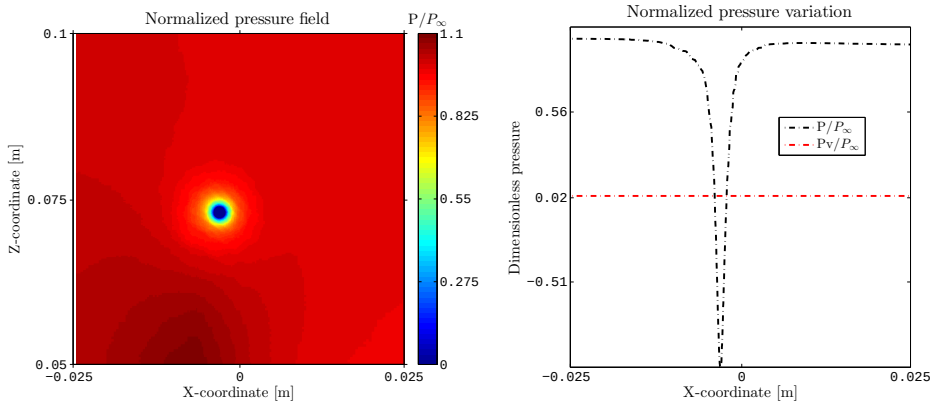

(a) Pressure (b) Pressure through core

Figure A.6: Pressure at 0.6c.

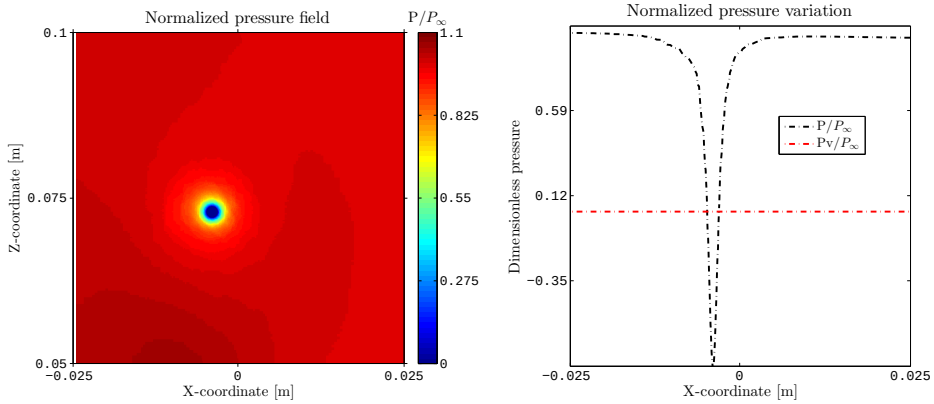

(a) Pressure (b) Pressure through core

Figure A.7: Pressure at 0.8c.

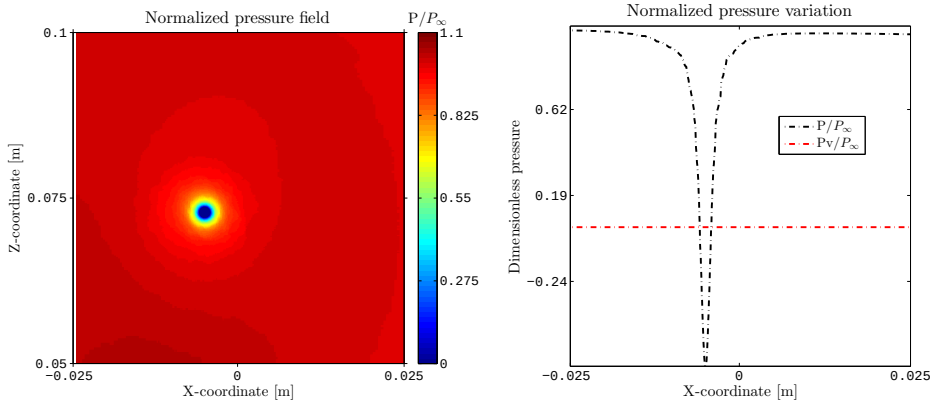

(a) Pressure (b) Pressure through core

Figure A.8: Pressure at 1.0c.

CAVITY RADIUS AND CENTER FREQUENCY

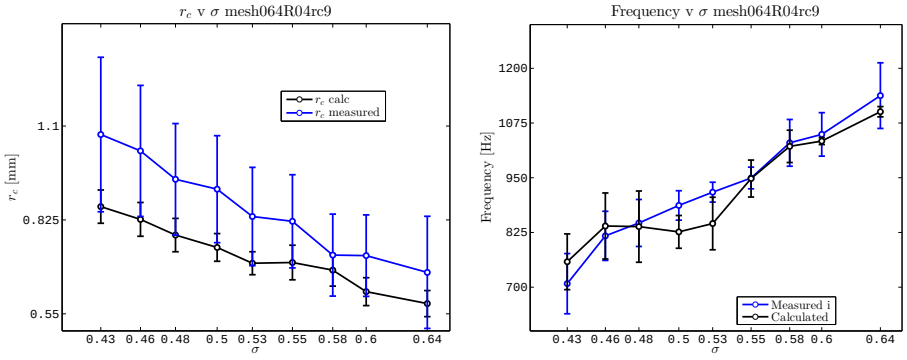

(a) r_c (b) f

Figure A.9: Cavity radius and center frequency at 0.4c.

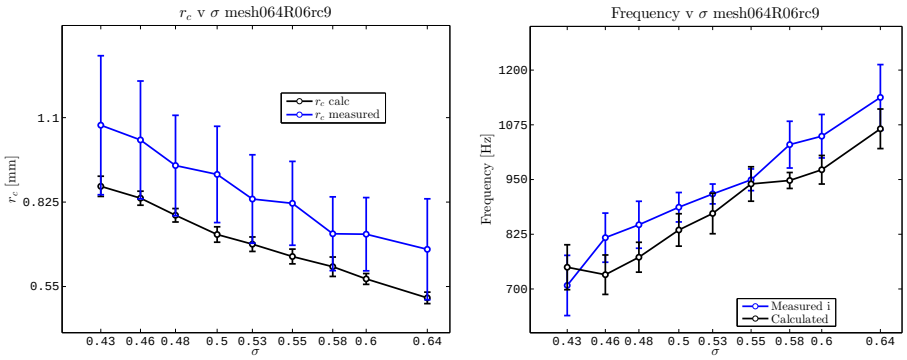

(a) r_c (b) f

Figure A.10: Cavity radius and center frequency at 0.6c.

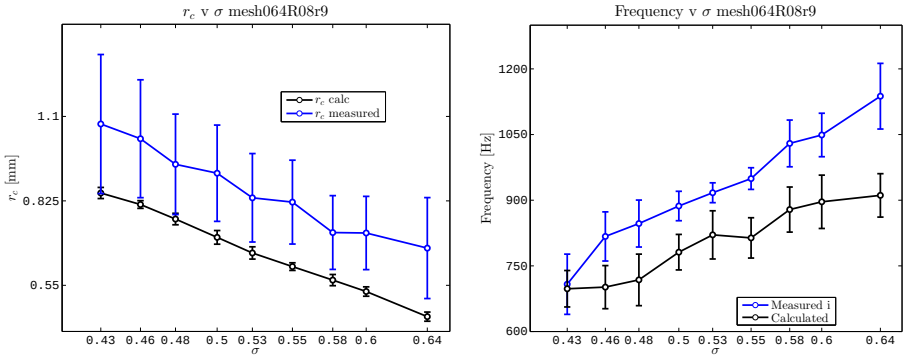

(a) r_c (b) f

Figure A.11: Cavity radius and center frequency at 0.8c.

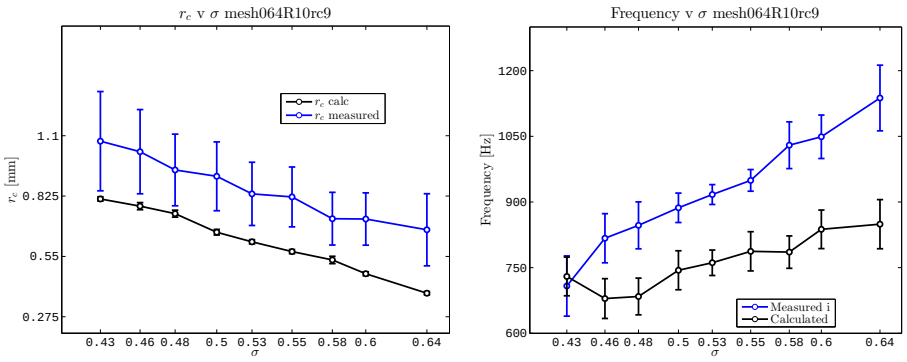

(a) r_c (b) f

Figure A.12: Cavity radius and center frequency at 1.0c.

MESH 0.80

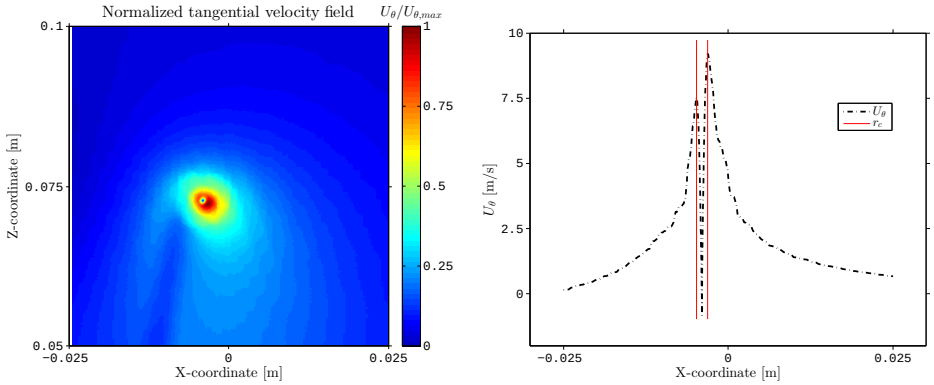

(a) U_θ (b) U_θ through core

Figure A.13: Tangential velocity at 0.8c.

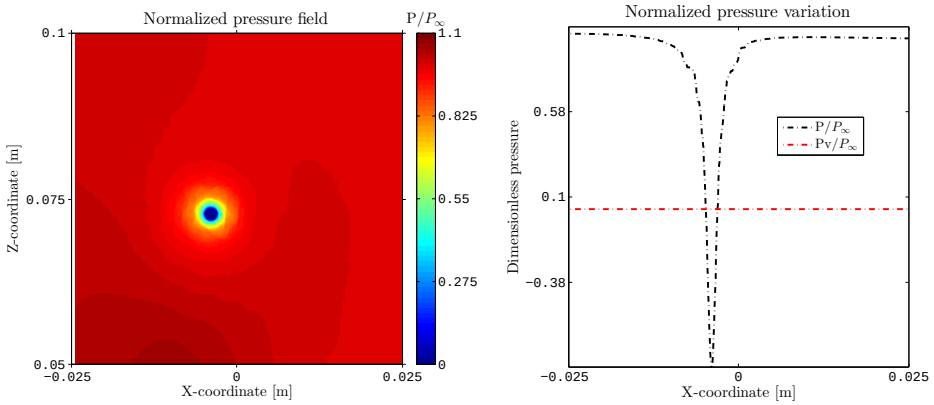

(a) Pressure (b) Pressure through core

Figure A.14: Pressure at 0.8c.

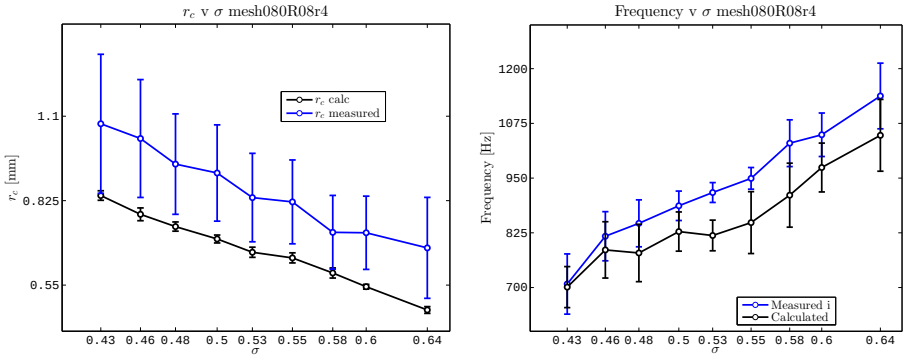

(a) r_c (b) f

Figure A.15: Cavity radius and center frequency at 0.8c.

MESH 1.0

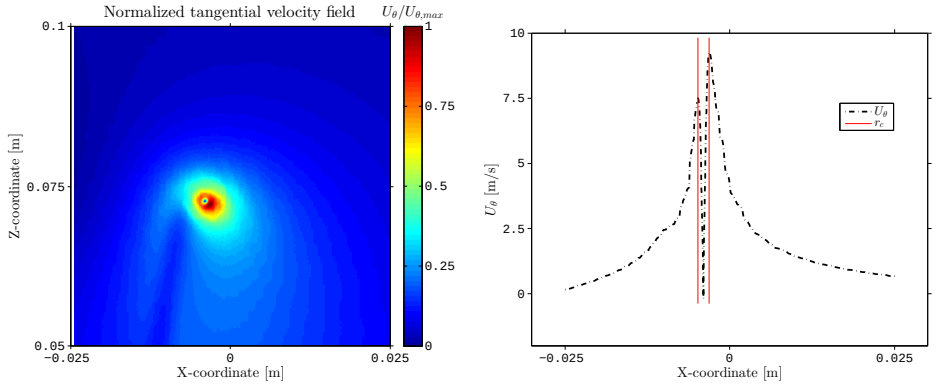

(a) U_θ (b) U_θ through core

Figure A.16: Tangential velocity at 0.8c.

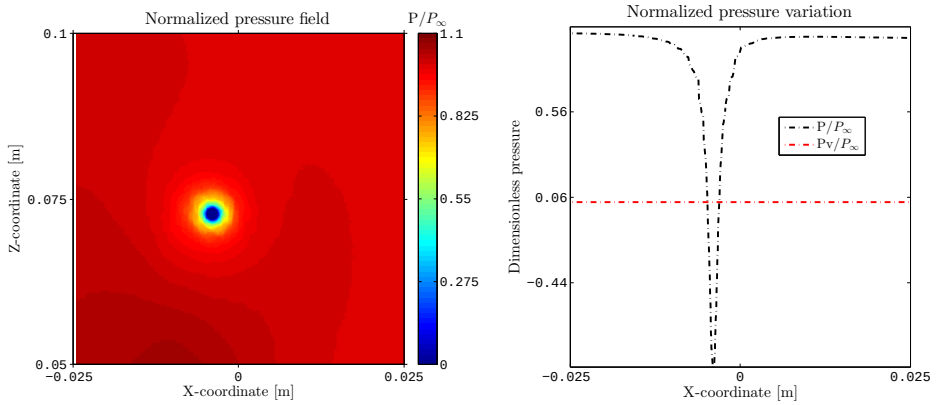

(a) Pressure (b) Pressure through core

Figure A.17: Pressure at 0.8c.

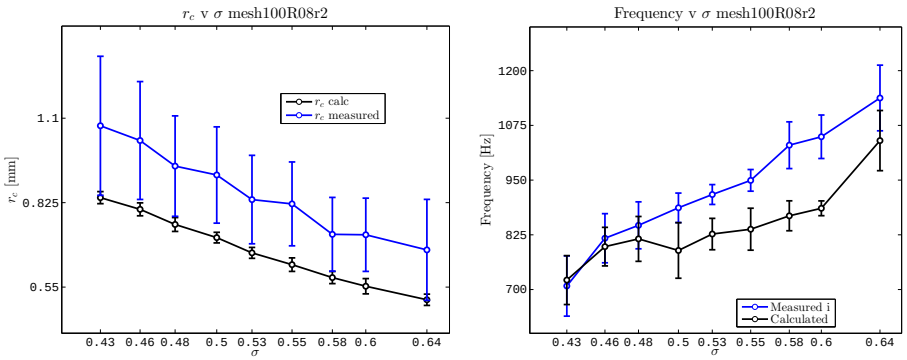

(a) r_c (b) f

Figure A.18: Cavity radius and center frequency at 0.8c.